Reconfigurable Intelligent Surface-Assisted Wireless Networks and Channel Modeling

by

Fatih Kılınç

A Dissertation Submitted to the
Graduate School of Sciences and Engineering
in Partial Fulfillment of the Requirements for
the Degree of

Master of Science

in

Electrical and Electronics Engineering

KOÇ ÜNİVERSİTESİ

September 15, 2022

Reconfigurable Intelligent Surface-Assisted Wireless Networks and Channel Modeling

Koç University

Graduate School of Sciences and Engineering

This is to certify that I have examined this copy of a master's thesis by

Fatih Kılınç

and have found that it is complete and satisfactory in all respects,

and that any and all revisions required by the final

examining committee have been made.

Committee Members:

Assoc. Prof. Ertuğrul Başar (Advisor)

Prof. Sinem Çöleri

Assoc. Prof. Mehmet Kemal Özdemir

Date:

Dedicated to my family and my lovely wife for their support and love.

ABSTRACT

Reconfigurable Intelligent Surface-Assisted Wireless Networks and Channel Modeling
Fatih Kılınç
Master of Science in Electrical and Electronics Engineering
September 15, 2022

Reconfigurable intelligent surface (RIS)-assisted communications is one of the promising candidates for next generation wireless networks by controlling the propagation environment dynamically. In this thesis, a channel modeling strategy for RIS-assisted wireless networks is introduced in sub-6 GHz bands by considering both far-field and near-field behaviours in transmission. We also proposed an open-source physical channel simulator for sub-6 GHz bands where operating frequency, propagation environment, terminal locations, RIS location and size can be adjusted. It is demonstrated via extensive computer simulations that an improved achievable rate performance is obtained in the presence of RISs for both near-field and far-field conditions. Furthermore, the spatial correlation between RIS elements are investigated in a millimeter wave (mmWave) transmission scenario.

Conventional power domain non-orthogonal multiple-accessing (PD-NOMA) scheme require transmission power allocation on the user side, which creates computational complexity and signaling overhead that hinders NOMA implementation. This thesis also introduce an RIS-assisted grant-free non-orthogonal multiple access (GF-NOMA) scheme. We propose a joint user equipment (UE) clustering and RIS assignment and alignment approach that ensures the power reception disparity required by the PD-NOMA. The proposed approach maximizes the network sum rate by judiciously pairing UE with distinct channel gains and assigning RISs to proper clusters. To alleviate the computational complexity of the joint approach, we decouple UE clustering and RIS assignment/alignment subproblems, which reduces run times 80 times while attaining almost the same performance. Once the proposed approaches acknowledge UEs with the cluster index, UEs are allowed to access corresponding resource blocks (RBs) at any time requiring neither further grant acquisitions from the base station (BS) nor power control as all UEs are requested to transmit at the same power. In addition the RIS assisted GF-NOMA scheme enhances the sum-rate of the network by 18% compared to conventional PD-NOMA which requires transmit power allocation at the UE side. Our numerical results also investigate the impact of UE density, RIS deployment, RIS hardware specifications, and the fairness among the UEs in terms of bit-per-joule energy efficiency.

Furthermore, this thesis introduces two hybrid transmission schemes combining a passive reconfigurable intelligent surface (RIS) with decode-and-forward (DF) relaying in a synergistic manner. The proposed schemes offer a flexible as well as cost- and power-efficient solution for coverage extension in future generation wireless networks. We present the end-to-end signal-to-noise ratio of both schemes and a sequential optimization algorithm for the power allocation and the RIS phase configurations. Our computer simulations demonstrate that the use of an RIS and relaying technologies enhance the achievable rate and error performance remarkably when working complementary to each other, rather than being considered as competing technologies.

ÖZETÇE

Yüksek Lisans Tez Başlığı

Fatih Kılınç
Elektrik ve Elektronik Mühendisliği, Yüksek Lisans

15 Eylül 2022

Yeniden yapılandırılabilir akıllı yüzey (RIS) destekli iletişim, yayılma ortamını dinamik olarak kontrol edebilen ve gelecek nesil kablosuz ağlar için umut verici adaylardan biridir. Bu tezde, iletimde hem uzak alan hem de yakın alan davranışları dikkate alınarak 6 GHz altı bantlarda RIS destekli kablosuz ağlar için bir kanal modelleme stratejisi tanıtılmaktadır. Ayrıca, çalışma frekansının, yayılma ortamının, terminal konumlarının, RIS konumunun ve boyutunun ayarlanabildiği 6 GHz altı bantlar için açık kaynaklı bir fiziksel kanal simülatörü önerdik. Kapsamlı bilgisayar simülasyonları ile, hem yakın alan hem de uzak alan koşulları için RIS'lerin varlığında iyileştirilmiş bir ulaşılabilir hız performansının elde edildiği gösterilmiştir. Ayrıca, bir milimetre dalga iletim senaryosunda RIS elemanları arasındaki uzamsal korelasyon araştırılmıştır.

Geleneksel PD-NOMA şemaları, NOMA uygulamasını engelleyen hesaplama karmaşıklığı ve sinyal yükü yaratan kullanıcı ekipmanı (UE) tarafında iletim gücü tahsisi gerektirir. Bu tez ayrıca, yeniden yapılandırılabilir bir akıllı yüzey (RIS) destekli hibesiz ortogonal olmayan çoklu erişim (GF-NOMA) şemasını tanıtmaktadır. Güç alanı NOMA'nın (PD-NOMA) gerektirdiği güç alımı eşitsizliğini sağlayan bir ortak UE kümelemesi ve RIS ataması ve faz ayarlama yaklaşımı öneriyoruz. Önerilen yaklaşım, UE'yi farklı kanal kazançlarıyla akıllıca eşleştirerek ve RIS'leri uygun kümelere atayarak toplam ağ oranını maksimuma çıkarır. Ortak yaklaşımın hesaplama karmaşıklığını hafifletmek için, hemen hemen aynı performansı elde ederken çalışma sürelerini 80 kat azaltan UE kümeleme ve RIS atama/ayarlama alt problemlerini ayırıyoruz. Önerilen yaklaşımlar küme indeksi ile UE'leri onayladıktan sonra, tüm UE'lerin aynı güçte iletim yapmaları istendiğinden, UE'lerin herhangi bir zamanda ne baz istasyonundan (BS) daha fazla hibe edinimi (BS) ne de güç kontrolü gerektirmeyen ilgili kaynak bloklarına (RB'ler) erişmesine izin verir. Ek olarak, RIS destekli GF-NOMA şeması, UE tarafında iletim gücü tahsisi gerektiren

geleneksel PD-NOMA'ya kıyasla ağın toplam hızını 18% oranında artırır. Sayısal sonuçlar ayrıca UE yoğunluğunun, RIS konuşlandırmasının, RIS donanım spesifikasyonlarının etkisini ve UE'ler arasındaki adilliği joule başına bit enerji verimliliği açısından ortaya koyar.

Ayrıca, bu tez, pasif yeniden yapılandırılabilir akıllı yüzey (RIS) ile kod çözme ve iletme tabablı röleleri sinerjik bir şekilde birleştiren iki hibrit iletim şemasını tanıtmaktadır. Önerilen şemalar, gelecek nesil kablosuz ağlarda kapsama alanının genişletilmesi amacıyla hem esnek hem de maliyet ve güç açısından verimli bir çözüm sunar. Her iki şemanın uçtan uca sinyal-gürültü oranını ve güç tahsisi ve RIS faz konfigürasyonları için sıralı bir optimizasyon algoritmasını sunulmuştur. Bilgisayar simülasyonları, RIS ve aktarma teknolojilerinin, rakip teknolojiler olarak görülmek yerine birbirini tamamlayıcı olarak çalışırken elde edilebilir veri oranını ve hata performansını önemli ölçüde artırdığını göstermektedir.

ACKNOWLEDGMENTS

I would like to express my sincere gratidute to my advisor Assoc. Prof. Ertuğrul Başar for his continous support and belief in me and guiding me through this journey. I am very grateful to be a part of his team CoreLab. I would like thank my friends and labmates for their support and motivation.

I would also like to thank my partners in science and my lifelong friends, Recep Akif Taşçı and Emre Arslan, who have always stood by me and overcome the problems together.

I would like to thank my dear family for their trust and support in me. They have always supported me wholeheartedly and given me strength on my journey.

Last but not least, I would like to thank my wife Ayşe Sena Kılınç for her endless love, support and pushing me to be a successful husband.

TABLE OF CONTENTS

LIST OF TABLES

LIST OF FIGURES

ABBREVIATIONS

AA	Axial Assignment
AF	Amplify-and-Forward
BS	Base Station
CSI	Channel State Information
DF	Decode-and-Forward
EE	Energy Efficiency
EM	Electromagnetic
eMBB	Enhanced Mobile Broadband
GB	Grant Based
GF	Grant Free
LoS	Line-of-Sight
MGF	Multi Level Grant Free
HD	Half Duplex
IM	Index Modulation
LSA	Linear Sum Assignment
MINLP	Mixed-integer Non-linear Programming
MIMO	Multiple-input Multiple-output
mMTC	Massive Machine-type Communications
NLoS	Non-Line-of-Sight
NOMA	Non-Orthogonal Multiple Access
OMA	Orthogonal Multiple Access
PD	Power Domain
PLS	Physical Layer Security
PUCCH	Physical UL Control Channel
PUSCH	Physical UL Shared Channel

RB	Resource Block
Rx	Receiver
RIS	Reconfigurable Intelligent Surface
SE	Spectral efficiency
SGF	Single Level Grant Free
SIC	Successful Interference Cancellation
SISO	Single-input Single-output
SRS	Sounding Reference Signal
STAR	Simultaneously Transmitting and Receiving
TDD	Time Division Duplex
Tx	Transmitter
UE	User Equipment
UL	Uplink
UpPTS	UL Pilot Time Slot
URRLC	Ultra-reliable Low Latency Communications
2D	Two Dimensional
3D	Three Dimensional
5G	Fifth Generation
6G	Sixth Generation

Chapter 1

INTRODUCTION

Next-generation communication networks are expected to meet rich services and use-cases, which are ultra-reliable low latency communications (URRLC), enhanced mobile broad- band (eMBB), and massive machine-type communications (mMTC). Although fifth-generation (5G) technology is a big step toward these goals, researchers continue to work on candidate technologies for beyond 5G networks to reach the expected limits for key performance metrics.

Reconfigurable intelligent surfaces (RISs) have emerged as a transformative technology envisioned for next-generation wireless networks to improve the spectral efficiency (SE) with low power consumption and hardware costs [Basar et al., 2019]. RISs have low-cost and low-power hardware as they consist of a large number of passive elements. The RIS controller manipulates the reflection of incident electromagnetic waves towards the desired direction by intelligently controlling the phase shift of elements [Basar et al., 2019]. The passive beamforming nature of RISs has been shown to improve network capacity [Basar et al., 2019, Arslan et al., 2022], enhance the end-to-end performance of multi-hop communications [Kilinc et al., 2021], and deliver a performance comparable to traditional relaying schemes [M.Di Renzo *et al.*, 2020]. RISs are also used cooperatively with existing technologies to assist and improve the networks capacity as well. Integration of the RIS concept with envisioned technologies for 5G such as non-orthogonal multiple access (NOMA) schemes, multiple-input multiple-output (MIMO) networks, index modulation (IM) techniques, coordinated multi-point transmission techniques, physical layer security (PLS), localization, detection and its common use with relays are also the subject of research. To express the benefits of RIS technology and realistically address the per-

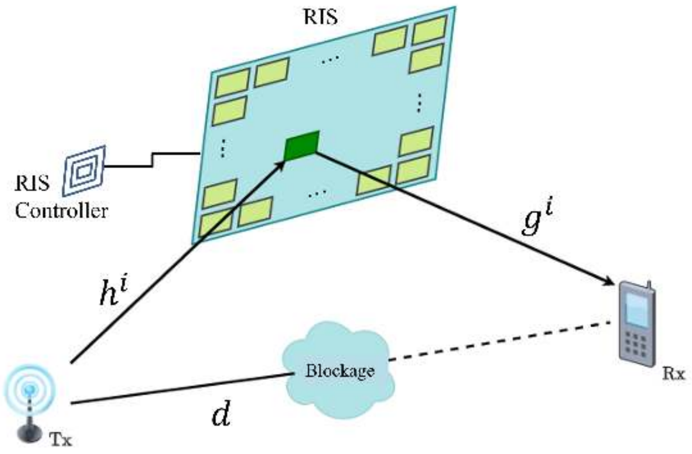

Figure 1.1: RIS assisted transmission model.

formance of RIS for different specifications in both far-field and near-field conditions, we need to come up with realistic channel models for RIS-assisted transmission. This thesis presents the following studies in the presence of RISs:

- RIS-assisted channel modeling in Sub-6 GHz bands
- Correlation analysis of the RIS-assisted channels in mmWave bands
- RIS-assisted grant-free NOMA
- Hybrid RIS & relay transmission schemes for non-ideal DF Relays

In-depth literature review will be given and the main contributions of the thesis will be explained in the next chapter. Here, the technologies that form the basis for the schemes proposed in the remainder of the thesis are briefly presented.

1.1 RIS Technology

RISs have recently received great attention due to their advantages in controlling the wireless propagation environment. An RIS is comprised of small electro-magnetic (EM) surfaces, which are capable of reflecting the incoming signals in a controllable and efficient way, and provides a more energy-efficient wireless communication network. The reflection properties of the EM surfaces can be dynamically controlled with nearly passive electronic components, called "meta-atoms". Considering all of these advantages of RIS, the implementation of an RIS in mmWave bands is one of the cost and power-efficient ways to enhance the system performance. The system model of an RIS assisted transmission is shown in Fig. 1.1. The channel coefficient between transmitter (Tx) and ith RIS element; Tx and receiver (Rx); ith RIS element and Rx are denoted by h^i,d, and g^i, respectively. Considering the reflections from all RIS elements, the received signal model can be written as:

$$y = \sqrt{P}\left(\sum_{i=1}^{N} h^i\phi^i g^i + d\right) s + w = \sqrt{P}\left(\sum_{i=1}^{N} |h^i||g^i| + d\right) s + w, \tag{1.1}$$

$$\phi^i = e^{j(\angle d - \angle h^i g^i)}, \tag{1.2}$$

where P, ϕ^i, s and w correspond to the transmit power, phase shift of the ith reflecting element, transmitted symbol and noise term. When the phases of RIS elements are designed to align the phases of the reflections from RIS elements with the phase of the direct path as in (1.2), the incoming signals from reflections and from the direct path are constructively added at the receiver side which increases the received signal power.

1.2 Decode-and-Forward Relays

Decode-and-Forward (DF) relays are regenerative network nodes. A DF relay first decodes the received signals and re-modulates and transmit to the destination. The half-duplex (HD) DF relays, decodes the received signal in the first time slot, and re-encodes and transmits in the second time slot as seen in Fig. 1.2. The channels between the Tx-relay, Tx-Rx and relay-Rx are represented by h, d and g, respectively. The received signal model at the receiver and relay in the first time slot is

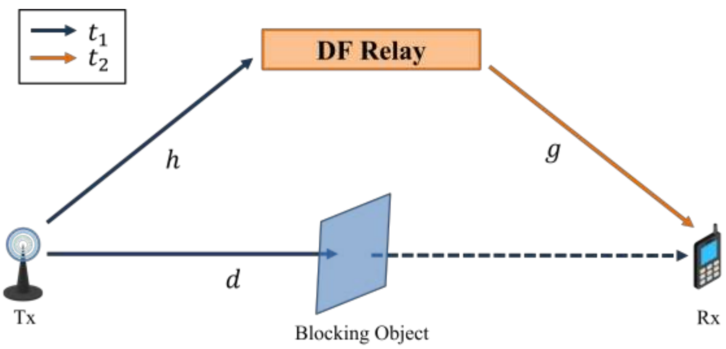

Figure 1.2: Relay-assisted transmission model.

expressed as:

$$y_d(t_1) = \sqrt{P_t} ds + w, \tag{1.3}$$

$$y_r(t_1) = \sqrt{P_t} gs + w, \tag{1.4}$$

where $y_d(t_1)$, $y_r(t_1)$ are the received signals at the Rx and at relay node in the first time slot (t_1), respectively. P_t, s and w denotes the transmit power of the Tx, transmitted symbol and the noise term, respectively. The relay decodes and re-encodes the received signal in t_1 and re-transmit at the second time slot (t_2). Therefore the received power at the Rx in the second time slot is modeled as:

$$y_d(t_2) = \sqrt{P_r} gs + w \tag{1.5}$$

where P_r, s and w are transmit power of the relay, transmitted symbol and the noise term, respectively. Since the DF relays do base-band processing, they are more complex and require signal processing capabilities compared to amplify-and-forward (AF) relays which basically amplifies the incoming signal in the RF domain and forwards to the receiver.

1.3 Non-Orthogonal Multiple Access

The next generation cellular networks should provide massive connectivity. Since we need to utilize the resources like communication bandwidth effectively for increasing number of users. Multiple accessing technologies aims to improve the capacity of a

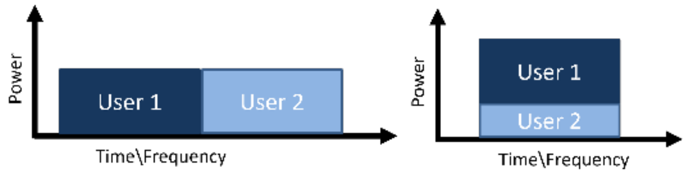

Figure 1.3: OMA compared to NOMA

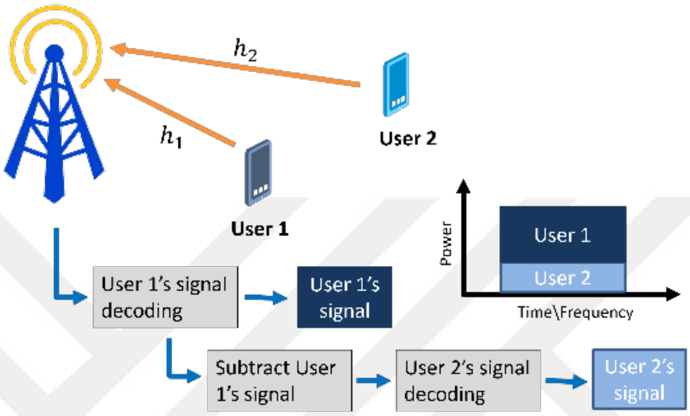

Figure 1.4: Uplink NOMA System Model

network and can be categorized into orthogonal multiple access (OMA) and NOMA techniques. In OMA, users share time/frequency resources, examples are TDMA and OFDMA. In NOMA systems users occupy the same time/frequency resources with different power levels. The main advantages of a NOMA system can enable the use of resources efficiently and can provide more connectivity compared to OMA systems. The comparison between the OMA and NOMA system and resource allocation are shown in Fig. 1.3. In this section we will focus on up-link (UL) power-domain NOMA system. The receiver distinguish the signals by their power levels and applies successive interference cancellation (SIC) since they are carried over same resource block. The system model of the UL-NOMA based transmission is shown in Fig. 1.4. The users transmit signals with different transmit powers and the received signals from the user 1 and user 2 is shown in Fig. 1.4. The channels between the user 1 to BS and user 2 to BS is denoted by h_1 and h_2, respectively. The received signal at the BS can written as:

$$y = \sqrt{P_{u1}} h_1 s + \sqrt{P_{u2}} h_2 s + w \tag{1.6}$$

where P_{u1}, P_{u2} and w are the transmit powers of user 1 and user 2; and the noise term, respectively. The BS applies SIC in which it first decodes the message of the strong user (user 1) by treating the weak user's (user 2) message as interference. Then BS subtracts the decoded message of the strong user from the received signal and decodes the message of the second user. Users need to adjust their transmit power according to each other's channel state information to create the required power disparity at the receiving node.

Chapter 2

LITERATURE REVIEW AND MAIN CONTRIBUTIONS

In this chapter, we will provide the in depth literature review about the existing technologies. Sections 2.1, 2.2 and 2.3 present the literature review on the RIS-assisted channel modeling, RIS and relay schemes, and the RIS-assisted and GF-NOMA networks, respectively. On top of that, we present the main contributions of the thesis to literature in section 2.4.

2.1 RIS-assisted Channel Modeling

Due to the developments in technology and the increase in data consumption, current communication systems have been inadequate to meet the increasing demands. Hence, next-generation wireless systems should provide data transfer at very high rates with a high reliability. Emerging technologies such as virtual-reality, high-quality streaming, and autonomous systems require novel ways to achieve higher data rates with low latency. Massive multiple-input multiple-output (mMIMO), millimeter wave (mmWave) communications, terahertz communications, and reconfigurable intelligent surfaces (RISs) can be considered as remarkable technologies for next-generation communication systems to enhance system performance[Basar et al., 2019].

RISs enable us to somehow control the propagation environment. an RIS is a nearly passive device comprises of small elements in the form of two-dimensional arrays. The reflection coefficient of RIS elements can be tuned by a controller. By controlling the phase response of these elements, we can align the phases of the reflections from RIS elements and add them constructively in the receiver side. RISs provides more energy-efficient communication network and can replace the power consuming nodes in the network. Considering all of these advantages of RIS, the implementation of an RIS in mmWave bands is one of the cost and power-efficient ways to enhance the system performance.

RISs have been extensively investigated in the literature from various aspects, where the physical properties, behaviours and different use cases of RISs, such as holographic beamformers, low complexity transmitters, anomalous reflectors are investigated [Basar et al., 2019, Huang *et al.*, 2020]. The integration of an RIS into currently existing technologies such as IM techniques and relay-aided systems are proposed in [Yildirim et al., 2021a] and [Basar, 2020]. Moreover, the efficient positioning and beamforming optimization of the RIS in MIMO networks are studied in [Wu et al., 2021] and [Zhang and Zhang, 2020]. Since carrier signals are vulnerable to blockage and suffer from path loss in mmWave communications, an RIS can be used to ensure reliable transmission by creating an additional path. Therefore, the most of the studies in the literature are focused on the deployment of RIS in mmWave frequencies. Modeling of the RIS-assisted wireless channels also stands out as another key direction for the research community. RISs are mostly designed in the form of uniform planar array (UPA), therefore, two dimensional (2D) channel models are not accurate for RIS-assisted networks. In this context, 3D physical channel models for RIS-assisted mmWave networks are proposed in several recent works [Basar et al., 2021, Basar and Yildirim, 2020, Yildirim et al., 2021b]. However, the RIS technology can also be used in sub-6 GHz bands, which is used for majority of wireless communication systems, such as 3G/4G and even 5G cellular networks, Wi-Fi systems in our homes, and bluetooth devices. The existing studies, which reveal the effects and behavior of RIS in sub-6 GHz bands, have not exhaustively investigated physical channels.

2.2 *RIS and Relay Schemes*

RIS-empowered wireless transmission has recently drawn substantial attention from both academia and industry [Basar and Yildirim, 2020, Di Renzo *et al.*, 2019, Yildirim et al., 2020]. There are many research efforts examining the differences between RIS and relaying technologies. Although RISs and relaying are similar technologies to enhance the system performance, the received signal is actively processed at the relay, while the RIS only reflects the incident signal without any active transmit module [Huang *et al.*, 2019]. In [Björnson et al., 2020], HD DF relaying and RIS-assisted transmission are compared in terms of energy efficiency, and it has been shown that the performance of a relay is achievable when hundreds of reflectors are used at the RIS. Moreover, a full-duplex (FD) relay-assisted system comprising two horn antennas and two RISs very close to the relay has been proposed in [Ying et al., 2020], and improvements in achievable rate are achieved even with a low number of reflective elements. However, the consideration of two horn antennas for the FD relay will cause high hardware cost, rendering end-to-end channel estimation difficult in the case of large numbers of transmission nodes and terminals. In [Abdullah *et al.*, 2020a], the authors proposed a hybrid transmission scenario combining a DF relay with an RIS and showed that using a single relay for low signal-to-noise ratio (SNR) values outperforms an RIS with massive number of reflectors, while for high SNRs, RIS-assisted transmissions are preferable. Recently in [Abdullah *et al.*, 2020b], RIS and FD relay are combined to provide reliable transmission and a semi-definite relaxation-based approach is proposed to cope with a non-convex optimization problem.

2.3 RIS-Assisted and Grant Free Non-Orthogonal Multiple Access

Non-orthogonal multiple access has also been recognized as a promising candidate to enable enhanced mMTC by multiplexing several user equipments (UEs) on the same network resources [Saito et al., 2013, Islam et al., 2017]. In particular, PD-NOMA improves the SE by multiplexing UEs with different channel gain and transmit power such that successive interference cancellation (SIC) can be performed at the receiver. As the network size increases, PD-NOMA starts suffering from power control complexity, UE pairing and resource allocation overhead and ramifications of channel state information (CSI) acquisition [Shahab et al., 2020]. NOMA has also been investigated with emerging technologies such as index modulation [Arslan et al., 2020], cognitive radios [Arzykulov et al., 2021], and unmanned aerial vehicles-aided wireless networks [Arzykulov et al., 2022]. Recently, RISs have received attention thanks to their ability to create the reception power disparity required by PD-NOMA. While the RIS-aided NOMA is analyzed in [Hou et al., 2020a], dynamic and static RIS configurations for multi-user NOMA schemes are considered in [Liu et al., 2022]. The authors of [Khaleel and Basar, 2022] have studied partitioning of RIS to facilitate PD-NOMA. Noting that all of the mentioned schemes are grant-based (GB), there is still a dire need to address the signaling overhead and computational complexity issues. For this reason, research on grant-free NOMA (GF-NOMA) schemes that UEs can operate without grant acquisition recently received much attention. In particular, power-domain GF-NOMA schemes aim to eliminate the need for power control and CSI acquisition at the Tx side so that UEs can access allocated resource blocks (RBs) at any time without requiring grant acquisition.

RIS-Assisted NOMA Networks: RISs have received attention thanks to their ability to create the reception power disparity required by PD-NOMA [C.Pan *et al.*, 2021]. The authors compare the RIS-assisted orthogonal multiple access (OMA) and NOMA technologies from different aspects and evaluate the performance of static and dynamic RISs in [Liu et al., 2022]. In [Hou et al., 2020b], the authors design passive beamforming weights to boost the performance of the PD-NOMA and propose a priority-oriented NOMA scheme to increase SE. In [Yang et al., 2021a], the authors aim to maximize the minimum signal-to-noise-plus-interference-ratio (SINR) threshold by deploying RISs in NOMA networks. Integration of the RIS technology to NOMA brings optimization problems such as joint optimal power allocation, RIS phase configuration, and UE allocation to obtain the best performance from the two technologies. To address these problems [Liu et al., 2021b] uses a two-step machine learning approach for joint deployment, phase shift design, and power allocation. Also, [Yang et al., 2021b] uses machine learning algorithms for UE partitioning and phase shifter network design. [Zhong et al., 2022] investigates the artificial intelligence empowered RIS-NOMA networks by using deep reinforcement learning. The existing literature also inspects RIS-NOMA schemes from the physical layer security perspective. In [Tang et al., 2021], authors propose novel RIS-assisted NOMA schemes for enhancing the physical layer security (PLS). The study in [Zhang et al., 2021] proposes sub-optimal joint beamforming and power allocation scheme to increase the PLS as well. The RISs are also used for serving cell-edge UEs by integrating RIS technology into joint transmission-coordinated multipoint in a two-cell NOMA-based network in [Elhattab et al., 2021]. Using different RIS designs and partitioning RIS into sub-surfaces are also proposed to serve multiple UEs simultaneously to employ NOMA. The authors in [Khaleel and Basar, 2022] propose RIS partitioning to employ NOMA and maximize UE fairness. Furthermore, [Aldababsa et al., 2022, Aldababsa et al., 2021] use simultaneously transmitting and receiving (STAR) RIS in NOMA networks and evaluate from an error performance perspective. The hardware impairments of the RIS also considered in the literature, and the effects on the outage probability [Hemanth et al., 2020] and secrecy rate [Chen et al., 2021] is investigated.

GF-NOMA Networks: GF access appears to be a savior technology for NOMA networks. GB NOMA networks require the UEs in the same cluster to know the CSI of other members and align their transmission power accordingly. This process also causes a considerable signaling overhead and computational complexity on the UE side. Therefore scientists are looking for ways to exclude the computation on the UE side and enable them to access the base station (BS) without grant permission. Multiple access based, compute and forward-based, compressed sensing-based GF-NOMA schemes are presented, and future directions of GF-NOMA technology are given in [Shahab et al., 2020]. The ALOHA-NOMA schemes are proposed in [Balevi et al., 2018, Elkourdi et al., 2018] which provide high throughput and lower complexity. Semi-GF schemes where GB and GF UEs share the same spectrum are evaluated from the stochastic geometry perspective in [Zhang et al., 2022, Zhang et al., 2020]. The authors analyze the compressing sensing-based GF-NOMA via stochastic geometry in [Liu et al., 2021a]. A transmit power pool with the help of a deep reinforcement learning algorithm is created for UEs at certain distances sharing the same RB in [Fayaz et al., 2021]. In [Abbas et al., 2019] a novel framework is proposed to avoid collusion in GF-NOMA networks when two UEs choose the same pilot sequence. Index modulation integrated GF-NOMA scheme for uplink (UL) transmission is presented in [Doğan et al., 2019]. In [Celik, 2021], the author presents low complexity multi-level and single GF-NOMA schemes and an UE clustering approach exploiting the channel gains of the UEs. RIS technology is used in [Chen et al., 2022] where authors propose a semi GF-NOMA scheme using deep reinforcement learning to control the transmit power and phase shifts. As pointed out by a recent survey on GF-NOMA [Shahab et al., 2020], RIS-aided GF-NOMA is a promising technology but has not been explored in-depth yet.

2.4 Main Contributions of the Thesis

The main contributions of this thesis can be categorized into three main parts. Chapter 3 presents a modeling strategy for RIS-empowered communication systems by considering the currently used technical specifications on sub-6 GHz bands [3GP, 2017, Kyösti *et al.*, 2008]. According to a common assumption in the literature, the most efficient use of an RIS is possible when it is placed close to the terminals. Since the wavelengths of the carriers in sub-6 GHz bands are significantly higher than those in mmWave bands, deployment of a large RIS in sub-6 GHz bands requires the RIS to operate in near-field if the RIS is placed close to Tx or Rx. In order to cover these use-cases, the impact of the RIS in both far-field and near-field conditions are analyzed in this chapter. Furthermore Chapter 3 analyzes the spatial correlation between the RIS elements in mm-wave bands in both indoor and outdoor environments. The analytic and semi analytic approaches are presented and compared with the simulation results. The results show that channels are highly correlated in an indoor environment compared an outdoor environment, and RIS structures with reduced correlation should be designed.

To the best of the authors' knowledge, Chapter 4 is first to introduce an RIS-assisted fully GF-NOMA scheme where the required power disparity is obtained by three levels of implicit power control: clustering UEs with different channel gains into the same cluster, properly assigning RISs to UE clusters to increase power reception disparity, and aligning the phase shift matrix of RISs according to the cluster members to reach the highest possible network sum rate. In this way, the proposed approaches perform an over-the-air power control by judiciously pairing UEs, assigning RISs, and aligning phase shifts of RISs. Since optimizing UE clustering and RIS assignment/alignment for the maximum network sum rate is a non-deterministic polynomial-time (NP)-Hard problem, we propose two solution methodologies. In the former, we develop an iterative approach where each iteration exploits a three-dimensional axial assignment (3D-AA) problem for joint UE clustering, RIS assignment, and phase shift alignment. Since 3D cost matrix generation complexity increases with the number of UEs and RISs, the latter method decouples UE clustering and RIS assignment/alignment subproblems, which yields 80 times faster completion time while reaching almost the same performance as the joint approach. The network-level simulations show that the proposed RIS-assisted GF-NOMA schemes outperform optimal GB PD-NOMA and regular GF-NOMA schemes. The RIS-assisted scheme provide %15 higher sum rate in a network where 150 UEs sharing 25 RBs, respectively. The network size simulation investigates the deployment scenarios, number of available RIS blocks and number of RIS elements. Deploying the RISs closer to the BS can yield up to %15 higher performance than a uniform distribution of the RISs across the cell area. The fairness among the UEs sharing the same RB is compared in terms of bit-per-joule energy efficiency by obtaining Jain's fairness index. The RIS-assisted scheme achieves the same fairness as regular GF-NOMA schemes while increasing the network capacity.

In Chapter 4, we introduce and propose two hybrid RIS and relay-assisted schemes as well as provide their working principles. Two novel hybrid transmission concepts are proposed by considering that an RIS and a DF relay are placed between the source (S) and the destination (D). It is assumed that the relay operates in HD mode, the RIS consists of N reflecting elements and the intelligent phase adjustment of the RIS is performed under perfect channel state information. Additionally, we propose a sequential power optimization algorithm under the non-ideal relay assumption.

Chapter 3

RIS ASSISTED CHANNEL MODELING

In this chapter, an RIS assisted channel modeling strategy in sub-6 GHz bands is presented in section 3.1. The spatial correlation analysis between RIS elements in mmWave bands is presented in section 3.2

3.1 RIS-assisted Channel Modeling in sub-6 GHz Bands

In this section, we will present the channel modeling strategy for RIS-assisted transmission in Sub-6 GHz bands. The effect and gains of RISs in sub-6 GHz bands are demonstrated by proposing a realistic channel model both in far-field and near-field conditions. The rest of this chapter can be summarized as follows. In Section 3.1.1, we propose RIS-assisted end-to-end channel model for indoor and outdoor environments operating in sub-6 GHz bands. In Section 3.1.2, we provide the achievable rate analysis of the system. In Section 3.1.3, the numerical results are presented.

3.1.1 System Model

In this section, we introduce our channel modeling strategy for RIS-assisted indoor and outdoor wireless communication systems in sub-6 GHz bands [Kilinc et al., 2021]. Proposed channel model for the RIS-empowered wireless network is established by considering the 3D channel modeling approach in 3GPP [3GP, 2017]. Additionally, the end-to-end single-input single-output (SISO) channel model is derived in the presence of an RIS. Furthermore, the near-field channel between the RIS-Rx is analyzed when the far-field conditions are not satisfied due to the close distance between the RIS-Rx. Since 2D channel models are not accurate for the RIS-assisted transmission owing to existence of an elevation angle, a 3D channel model should be taken into consideration. The considered propagation environments are Indoor

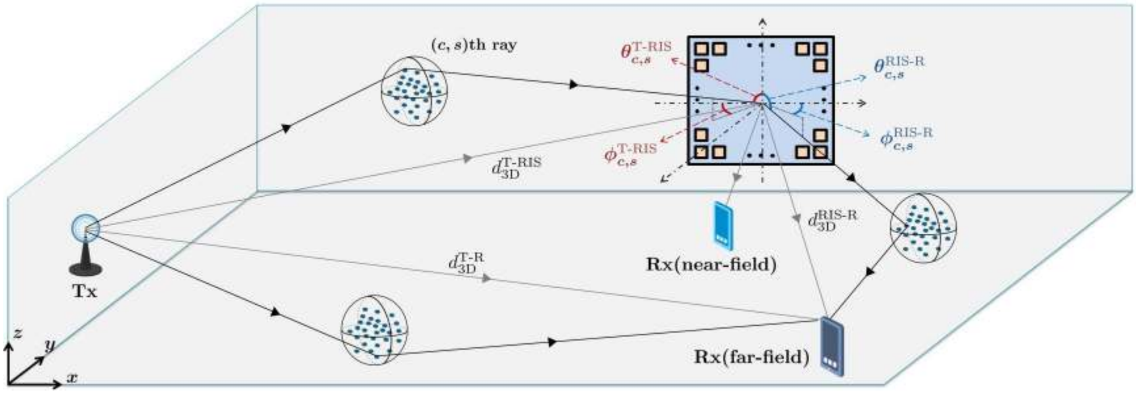

Figure 3.1: Generic system model for an RIS-assisted network with C number of clusters and S number of rays.

Hotspot (InH) and Urban Microcellular (UMi) in this chapter. The generic system model for the RIS-assisted wireless communication system is illustrated in Fig. 3.1, where $d_{3D}^{\text{T-RIS}}$,$d_{3D}^{\text{T-R}}$ and $d_{3D}^{\text{RIS-R}}$ represents the 3D distances between the Tx-RIS, Tx-Rx and RIS-Rx, respectively. It is assumed that the RIS with N number of elements is positioned on the xz-plane. There exist C clusters in the environment, each containing S rays. The channels between the Tx-RIS, RIS-Rx and Tx-Rx are denoted by $\mathbf{h} \in \mathbb{C}^{N\times 1}$, $\mathbf{g} \in \mathbb{C}^{N\times 1}$, and $h_{\text{SISO}} \in \mathbb{C}^{1\times 1}$, respectively, where N is the number of RIS elements. It is assumed that the Tx and Rx are equipped with unity gain isotropic antennas. The positions of the Tx, Rx and RIS are given in the cartesian coordinate system as $\mathbf{r}^{\text{Tx}} = (x^{\text{Tx}}, y^{\text{Tx}}, z^{\text{Tx}})$, $\mathbf{r}^{\text{Rx}} = (x^{\text{Rx}}, y^{\text{Rx}}, z^{\text{Rx}})$ and $\mathbf{r}^{\text{RIS}} = (x^{\text{RIS}}, y^{\text{RIS}}, z^{\text{RIS}})$, respectively. Considering the direct path and RIS reflection paths, the baseband equivalent of the received symbol at the Rx is expressed as

$$y = \sqrt{P_t}(\mathbf{g}^{\text{T}}\mathbf{\Theta}\mathbf{h} + h_{\text{SISO}})s + w \tag{3.1}$$

where P_t is the transmit power, s is the transmitted symbol, w is additive white Gaussian noise at the Rx, which is modeled as $w \sim \mathcal{CN}(0, N_0)$, and $(\cdot)^{\text{T}}$ denotes the transpose of the vector or matrix. The response matrix of the RIS is expressed as $\mathbf{\Theta} = \text{diag}(\beta_1 e^{j\alpha_1}, \cdots, \beta_N e^{j\alpha_N})$, where β_n and α_n represents the magnitude and the phase shift of the nth RIS element for $n = 1, 2, \ldots, N$, respectively.

Codes available at: https://github.com/fakilinc/RIS-Empowered-Sub-6-Ghz

3.1.1.1 Tx-RIS Channel

In this subsection, the channel between the Tx and RIS is presented and the channel generation procedure is explained in detail. The channel $\mathbf{h}$ is expressed as

$$\mathbf{h} = \sum_{c=1}^{C}\sum_{s=1}^{S}\sqrt{\frac{P_c}{S}}\sqrt{\frac{G_e(\theta_{c,s}^{\text{T-RIS}})}{P_L}}e^{j\Phi_{c,s}}\mathbf{a}(\theta_{c,s}^{\text{T-RIS}},\phi_{c,s}^{\text{T-RIS}}) \tag{3.2}$$

where P_c, $G_e(\theta_{c,s}^{\text{T-RIS}})$ and P_L are the power of the nth cluster, radiation pattern of an RIS element in the direction of (c, s)th path and the path loss component, respectively. Here, $\Phi_{c,s}$, $\theta_{c,s}^{\text{T-RIS}}$, and $\phi_{c,s}^{\text{T-RIS}}$ also represent the random initial phase, zenith angle of arrival (ZoA) and azimuth angle of arrival (AoA) of the RIS for the (c, s)th path, respectively. The array response vector of the RIS is also denoted by $\mathbf{a}(\theta_{c,s}^{\text{T-RIS}},\phi_{c,s}^{\text{T-RIS}})$. Considering these parameters, the generation steps of the Tx-RIS channel are listed as follows:

1) First, we need to set the environment and the locations of the Tx and RIS. The line-of-sight (LOS) ZoA ($\theta_{LOS}^{\text{T-RIS}}$) and AoA ($\phi_{LOS}^{\text{T-RIS}}$) angles is calculated by using the locations of the Tx and RIS.

2) Then, we need to assign propagation conditions (LOS/NLOS) and calculate the path loss P_L. The LOS probabilities for InH and UMi scenarios are calculated as given in [3GP, 2017, Table 7.2.2]. In addition, we assume 100% LOS probability, if the RIS is located at the same elevation or higher than the Tx as ($z^{\text{RIS}} \geq z^{\text{Tx}}$). Reference path loss models [3GP, 2017] for LOS (P_L^{LOS}) and NLOS (P_L^{NLOS}) cases in the InH environment are given as follows, respectively:

$$P_L^{\text{LOS}}[\text{dB}] = 16.9\log_{10}(d_{\text{3D}}) + 32.8 + 20\log_{10}(f_c) + \sigma_{SF}, \tag{3.3}$$

$$P_L^{\text{NLOS}}[\text{dB}] = 43.3\log_{10}(d_{\text{3D}}) + 11.5 + 20\log_{10}(f_c) + \sigma_{SF}. \tag{3.4}$$

Reference path loss models [3GP, 2017] for LOS and NLOS cases in the outdoor UMi environment are given as follows, respectively:

$$P_L^{\text{LOS}}[\text{dB}] = 22\log_{10}(d_{\text{3D}}) + 28 + 20\log_{10}(f_c) + \sigma_{SF}, \tag{3.5}$$

$$P_L^{\text{NLOS}}[\text{dB}] = 36.7\log_{10}(d_{\text{3D}}) + 22.7 + 26\log_{10}(f_c) - 0.3(h_{UT} - 1.5) + \sigma_{SF}. \tag{3.6}$$

In (3.3)-(3.6), f_c is the operating frequency in GHz, σ_{SF} is the shadow fading term and h_{UT} is the effective receive antenna height, which is the height of the RIS obtained by $h_{UT} = z^{\text{RIS}} - 1$. Here, d_{3D} is equivalent to $d_{\text{3D}}^{\text{T-RIS}}$ and calculated by $d_{\text{3D}}^{\text{T-RIS}} = \|\mathbf{r}^{\text{Tx}} - \mathbf{r}^{\text{RIS}}\|$.

3) Correlated large scale parameters should be generated. Shadow fading (SF), Ricean K factor, delay spread (DS), azimuth spread of arrival (ASA), azimuth spread of departure (ASD), zenith spread of arrival (ZSA), and zenith spread of departure (ZSD) are generated by considering the cross correlation coefficients between each other given in [3GP, 2017, Table 7.3-6].

4) The delays and the cluster powers should be generated. The delay associated with the cth cluster is given as τ_c and randomly generated by using exponential power delay distribution [3GP, 2017]. The cluster powers depend on the cluster delays and follow an exponential power delay profile. The power of the cth cluster is denoted by P_c and calculated as in [3GP, 2017]. Under LOS condition, the path from the first cluster is considered as the LOS path. Hence, the power of the LOS component ($P_{LOS} = K_R/(K_R+1)$) is added to the first cluster power and the power of the cth cluster is rewritten as

$$P_c = P_c/(K_R + 1) + \delta(c-1)P_{LOS} \tag{3.7}$$

where K_R is the Ricean factor in linear scale and $\delta(.)$ is the dirac delta function.

5) The ZoA ($\theta_{c,s}^{\text{T-RIS}}$) and AoA ($\phi_{c,s}^{\text{T-RIS}}$) angles of the RIS should be generated. Here, $\theta_{c,s}^{\text{T-RIS}}$ follows Laplacian distribution in both indoor and outdoor environments, and $\phi_{c,s}^{\text{T-RIS}}$ follows Laplacian distribution for indoors while it follows Wrapped Gaussian distribution for outdoors. The detailed generation process for $\theta_{c,s}^{\text{T-RIS}}$ and $\phi_{c,s}^{\text{T-RIS}}$ is explained in [3GP, 2017, sec. 7.3]. Additionally, $\theta_{c,s}^{\text{T-RIS}}$ is distributed within the range of $[0^\circ, 180^\circ]$, while $\phi_{c,s}^{\text{T-RIS}}$ is distributed within the range of $[-180^\circ, 180^\circ]$. Here, we need to ignore clusters behind the RIS by limiting the range of $\phi_{c,s}^{\text{T-RIS}}$ to $[0^\circ, 180^\circ]$.

6) The initial random phase for the (c, s)th path should be generated, where c is the cluster index and s is the ray index in each cluster. Here, $\Phi_{c,s}$ follows an uniform distribution as $\Phi_{c,s} \sim \mathcal{U}(-\pi, \pi)$.

7) The radiation pattern of the RIS elements should be calculated. We consider the $\cos^q$ radiation pattern, which is used for reflectarray antennas [Nayeri et al., 2018a] to model the radiation of the RIS elements. The radiation pattern in the direction of the (c, s)th path is calculated as

$$G_e(\theta_{c,s}^{\text{T-RIS}}) = 2(2q+1)\cos^{2q}(90 - \theta_{c,s}^{\text{T-RIS}}) \tag{3.8}$$

where $2(2q+1)$ is normalization factor and q is obtained as $q = 0.285$ in [Basar and Yildirim, 2020] by considering the physical area of RIS elements.

8) The array response vector of the RIS $\mathbf{a}(\theta_{c,s}^{\text{T-RIS}}, \phi_{c,s}^{\text{T-RIS}}) \in \mathbb{C}^{N\times 1}$ should be calculated. Here, a square RIS structure is considered and the horizontal/vertical distances between the elements are equal and denoted by d. As illustrated in Fig. 3.2, the ZoA and AoA angles to the RIS are $\theta_{c,s}^{\text{T-RIS}}$ and $\phi_{c,s}^{\text{T-RIS}}$, respectively. Considering the RIS geometry in Fig. 3.2, the first RIS element with the location vector $\mathbf{r}^1 = (x^1, y^1, z^1)$ is positioned at the bottom left corner of the RIS. $\mathbf{r}^n = (x^n, y^1, z^n)$ denotes the location vector of the nth RIS element, and x^n and y^n are respectively calculated as

$$\begin{aligned} x^n &= x^1 + d \cdot \text{ mod } \left(n-1, \sqrt{N}\right), \\ z^n &= z^1 + d \cdot \left\lfloor (n-1)/\sqrt{N} \right\rfloor \end{aligned} \tag{3.9}$$

where mod (.) is the modulus operation and $\lfloor . \rfloor$ is the floor operation. The normalized location of the nth RIS element according to first element is denoted by $(\overline{x}_n, 0, \overline{z}_n)$, where $\overline{x}_n = x^n - x^1$ and $\overline{z}_n = z^n - z^1$. The array response vector for an RIS with N elements is obtained by

$$\begin{aligned} \mathbf{a}(\theta_{c,s}^{\text{T-RIS}}, \phi_{c,s}^{\text{T-RIS}}) = \Big[1 \ \cdots \ e^{j\frac{2\pi}{\lambda}(\overline{x}_n \cos\theta_{c,s}^{\text{T-RIS}} + \overline{z}_n \sin\theta_{c,s}^{\text{T-RIS}} \cos\phi_{c,s}^{\text{T-RIS}})} \\ \cdots e^{j\frac{2\pi}{\lambda}(\overline{x}_N \cos\theta_{c,s}^{\text{T-RIS}} + \overline{z}_N \sin\theta_{c,s}^{\text{T-RIS}} \cos\phi_{c,s}^{\text{T-RIS}})}\Big]^{\text{T}} \end{aligned} \tag{3.10}$$

where λ is the wavelength of the carrier signal for $n = 1, \cdots, N$.

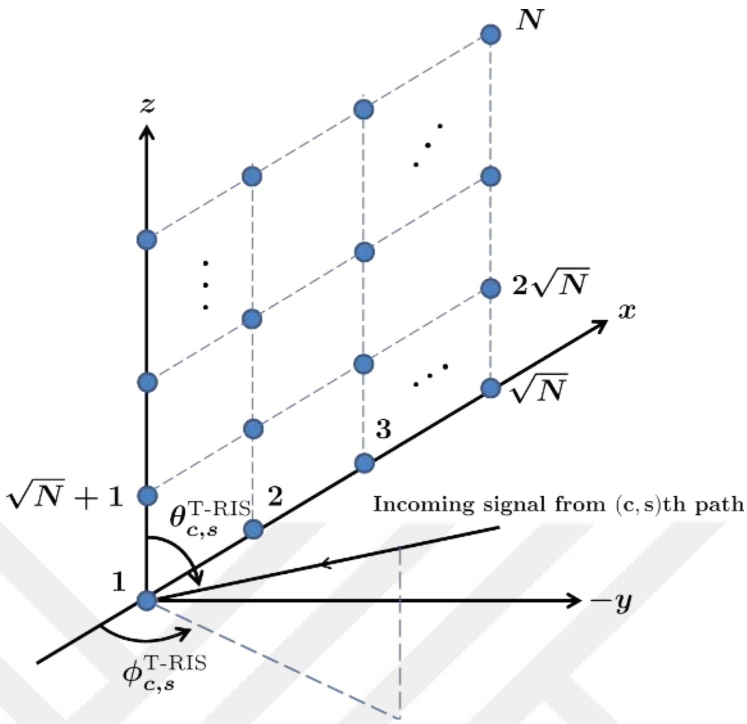

Figure 3.2: 3D RIS geometry.

Finally, we can form the channel **h** by using the channel parameters obtained in channel generation steps.

3.1.1.2 Tx-Rx Channel

The direct link between the Tx and Rx is given by

$$h_{\mathrm{SISO}} = \sum_{c=1}^{C}\sum_{s=1}^{S}\sqrt{\frac{P_c}{S}}\sqrt{\frac{1}{P_L}}e^{j\Phi_{c,s}} \tag{3.11}$$

where P_c, P_L and $\Phi_{c,s}$ is defined as in (3.2). h_{SISO} can be obtained by following the Steps 1, 2, 3, 4 and 6 in the channel generation procedure described in Tx-RIS channel subsection. In all steps, the Tx and Rx positions should be taken into account instead of Tx and RIS positions, respectively. Also, calculations for AoA and ZoA angles are not required in the generation process of h_{SISO}, since a SISO link established.

3.1.1.3 RIS-Rx Channel

For the RIS-Rx channel, we consider two different channel scenarios between the RIS and Rx. When the size of the RIS is large enough, the far-field distance between the RIS and Rx becomes significantly large. Therefore, the near-field channels are also considered in this section when the RIS is placed close to the Rx, while far-field channels are obtained by following the same procedure in previous sections.

Far-Field Channel:

The far-field channel $\mathbf{g}$ is given as

$$\mathbf{g} = \sum_{c=1}^{C} \sum_{s=1}^{S} \sqrt{\frac{P_c}{S}} \sqrt{\frac{G_e(\theta_{c,s}^{\text{RIS-R}})}{P_L}} e^{j\Phi_{c,s}} \mathbf{a}(\theta_{c,s}^{\text{RIS-R}}, \phi_{c,s}^{\text{RIS-R}}) \tag{3.12}$$

where P_c, P_L, and $\Phi_{c,s}$ is defined as in (3.2) and $G_e(\theta_{c,s}^{\text{RIS-R}})$ is the RIS element radiation pattern in the direction of (c, s)th path. The azimuth of departure (AoD) and zenith of departure (ZoD) angles from the RIS are represented by $\phi_{c,s}^{\text{RIS-R}}$ and $\theta_{c,s}^{\text{RIS-R}}$, respectively. The array response vector of the RIS is denoted by $\mathbf{a}(\theta_{c,s}^{\text{RIS-R}}, \phi_{c,s}^{\text{RIS-R}})$. The far-field channel can be produced by following the similar channel generation steps in Subsection II.A. In all steps, the RIS and Rx positions should be taken into account instead of Tx and RIS positions, respectively. In Steps 5, 7 and 8, the angles $\theta_{c,s}^{\text{RIS-R}}$ and $\phi_{c,s}^{\text{RIS-R}}$ should be considered instead of $\theta_{c,s}^{\text{T-RIS}}$ and $\phi_{c,s}^{\text{T-RIS}}$, and they follow the same distributions with $\theta_{c,s}^{\text{T-RIS}}$ and $\phi_{c,s}^{\text{T-RIS}}$, respectively. Additionally, $\theta_{c,s}^{\text{RIS-R}}$ is distributed within the range of $[0°, 180°]$, while $\phi_{c,s}^{\text{RIS-R}}$ is distributed within the range of $[-180°, 180°]$. Here, we need to ignore clusters behind the RIS by limiting the range of $\phi_{c,s}^{\text{RIS-R}}$ to $[0°, 180°]$ as in Subsection II.A.

Near-Field Channel:

In sub-6 GHz bands, the far-field distance, which is calculated by $\frac{N\lambda}{2}$ for a square RIS structure, increases significantly for larger RIS sizes. The scenarios, where the RIS is located in the far-field area, will be inefficient due to the high distance and multiplicative path loss. Hence, the near-field channels should be considered to analyze the RIS performance in near-field conditions. When the RIS operates in the near-field of Rx, there will be a pure LOS link between the RIS and Rx. Unlike far-field channels, the effective area of each RIS element changes since the angle of view of each RIS element to the Rx changes. Moreover, the distances from the RIS elements to the Rx varies. Furthermore, the polarization mismatch between the RIS elements should be taken into account under the near-field conditions[Björnson and Sanguinetti, 2020]. The near-field channel between the RIS and Rx is denoted by $\mathbf{g} = [g_1, g_2, \cdots, g_N]^{\mathrm{T}}$, where g_n represents the channel coefficient from the nth RIS element to the Rx, and can be expressed in terms of its magnitude and phase as $g_n = |g_n|e^{-j\gamma}$ for $n = 1, 2, \ldots, N$. By considering the RIS geometry in Fig. (3.2) and the RIS element locations in (3.9), the near field channel gain from the nth RIS element is approximated as according to [Björnson and Sanguinetti, 2020]

$$|g_n|^2 \approx \frac{1}{4\pi} \sum_{x\in\mathbb{X}} \sum_{z\in\mathbb{Z}} \left(\frac{\frac{xz}{y^2}}{3\left(\frac{z^2}{y^2}+1\right)\sqrt{\frac{x^2}{z^2}+\frac{z^2}{y^2}+1}} + \frac{2}{3}\tan^{-1}\left(\frac{\frac{xz}{y^2}}{\sqrt{\frac{x^2}{y^2}+\frac{z^2}{y^2}+1}}\right)\right) \tag{3.13}$$

where $\mathbb{X} = \left\{d/2 + x^n - x^{\mathrm{Rx}}, d/2 + x^{\mathrm{Rx}} - x^n\right\}$, $\mathbb{Z} = \left\{d/2 + z^n - z^{\mathrm{Rx}}, d/2 + z^{\mathrm{Rx}} - z^n\right\}$, and $y = |y^n - y^{\mathrm{Rx}}|$. The phase of g_n can be calculated as follows:

$$\gamma = 2\pi \bmod \left(\frac{\|\mathbf{r}^n - \mathbf{r}^{\mathrm{Rx}}\|}{\lambda}, 1\right). \tag{3.14}$$

3.1.2 Achievable Rate Analysis

In this section, we analyze the achievable rate of the RIS-assisted communication systems by optimally adjusting the phases of the RIS elements according to the channel conditions. We assume that the magnitude response is $\beta_n = 1$ for all RIS elements. The optimum phase response of the nth RIS element to maximize the signal-to-noise ratio (SNR) at the Rx is given by

$$\alpha_n = \arg(h_{\mathrm{SISO}}) - \arg(h_n g_n) \tag{3.15}$$

where $\arg(\cdot)$ denotes the phase of a complex number, h_n and g_n are the nth elements of $\mathbf{h}$ and $\mathbf{g}$, respectively. By considering the phase response in (3.15) for the RIS

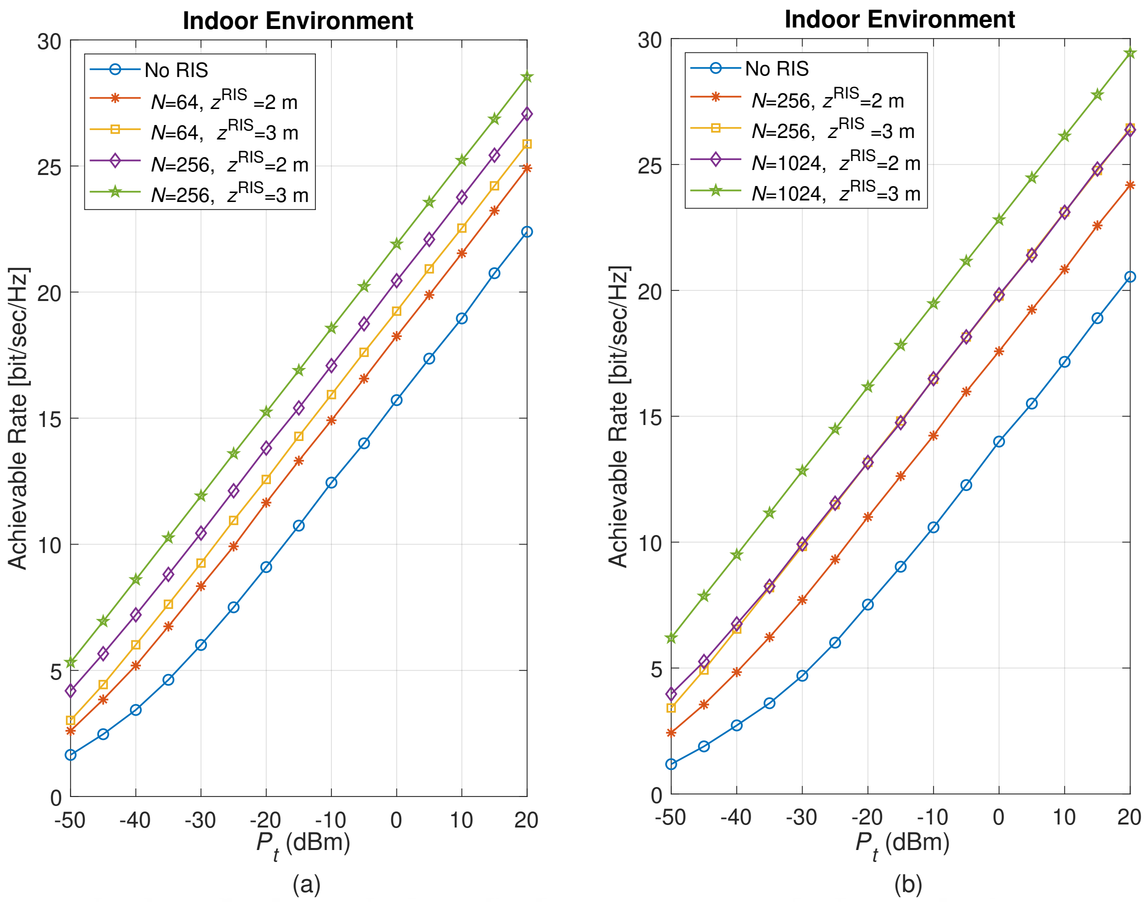

Figure 3.3: Achievable rates of RIS-assisted system for the indoor environment.

elements, the instantaneous received SNR is expressed as

$$\rho = \frac{P_t|\mathbf{g}^{\mathrm{T}}\mathbf{\Theta}\mathbf{h} + h_{\mathrm{SISO}}|^2}{N_0} = \frac{P_t\left|\sum_{n=1}^{N}|h_n||g_n| + h_{\mathrm{SISO}}\right|^2}{N_0}. \tag{3.16}$$

The maximized achievable rate of the system can be computed by $R = \log_2(1+\rho)$.

3.1.3 Simulation Results

In this section, we provide computer simulation results for the RIS-assisted transmission in sub-6 GHz bands. The achievable rate of the RIS-assisted communication systems is investigated for different scenarios. The noise power (N_0) is set to -130 dBm for all simulations.

In Figs. 3.3(a) and (b), the achievable rates are presented for varying N and different positions of the Tx, Rx and RIS for the indoor office environment. In both cases, the RIS is positioned in the near-field of the Rx, therefore, the near-field

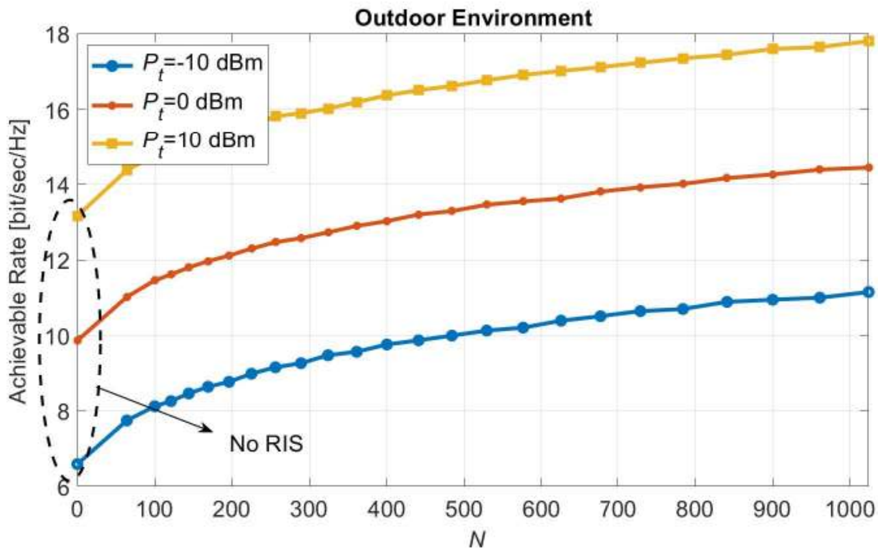

Figure 3.4: Achievable rates of RIS-assisted system for the outdoor environment.

channels are considered for the RIS-Rx link under 2.4 GHz operating frequency. In Fig. 3.3(a), the considered 3D coordinates are $\mathbf{r}^{\mathrm{Tx}} = (0, 25, 3)$, $\mathbf{r}^{\mathrm{Rx}} = (40, 48, 1.5)$ and $\mathbf{r}^{\mathrm{RIS}} = (38, 50, z^{\mathrm{RIS}})$, while $\mathbf{r}^{\mathrm{Tx}} = (0, 25, 3)$, $\mathbf{r}^{\mathrm{Rx}} = (67, 45, 1.5)$ and $\mathbf{r}^{\mathrm{RIS}} = (70, 50, z^{\mathrm{RIS}})$ in Fig. 3.3(b). The achievable rate analysis is presented depending on the height of RIS in both scenarios. When the Tx and RIS are in the same elevation in case $z^{\mathrm{RIS}} = 3$ m, we assume 100% LOS probability between the Tx and RIS. However, the LOS condition is not guaranteed in case $z^{\mathrm{RIS}} = 2$ since RIS is positioned below the Tx. According to Figs. 3.3(a) and (b), the achievable rate of the system is significantly better for the case $z^{\mathrm{RIS}} = 3$. Furthermore, the achievable rate of the system further increases as N increases. In Fig. 3.4, the effect of N on the achievable rate is investigated in the outdoor environment. We consider 2.4 GHz operating frequency and the 3D coordinates as $\mathbf{r}^{\mathrm{Tx}} = (0, 25, 10)$, $\mathbf{r}^{\mathrm{Rx}} = (65, 52, 1)$ and $\mathbf{r}^{\mathrm{RIS}} = (62, 55, 7)$. Here, near-field channels are considered for the RIS-Rx link, since the RIS operates in the near-field of the Rx by increasing N. As seen from the Fig. 3.4, the improved achievable rate is obtained for increasing N values. From the given results of Fig. 3.4, we observe that an RIS-assisted system with a sufficient number of RIS elements can outperform a system without RIS, which consumes 10 dB more transmit power.

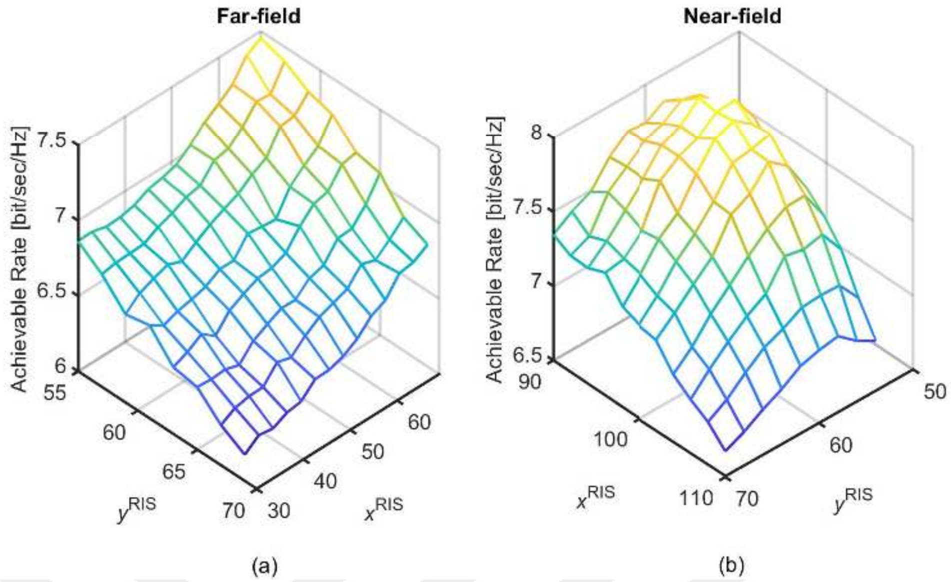

Figure 3.5: Achievable rates of RIS-assisted system for outdoors operating in (a) far-field and (b) near-field of Rx.

In Figs. 3.5(a) and (b), the achievable rate of the system is presented under various RIS positions for the outdoor environment. We consider the operating frequency of 5.8 GHz, $N = 1024$, and the 3D locations as $\mathbf{r}^{\mathrm{Tx}} = (0, 25, 10)$, $\mathbf{r}^{\mathrm{Rx}} = (100, 50, 1)$ and $\mathbf{r}^{\mathrm{RIS}} = (x^{\mathrm{RIS}}, y^{\mathrm{RIS}}, 7)$. In Fig. 3.5(a), the RIS is operating in the far-field of the Rx, therefore, far-field channels are considered for the RIS-Rx link. As seen in Fig. 3.5, the achievable rate of the system increases as the RIS gets closer to the Rx in both x and y-axes. Hence, the achievable rate of the system is maximized when $d_{\mathrm{3D}}^{\mathrm{RIS\text{-}R}}$ is minimized. When the RIS positioned in front of the Rx and operates in the near-field of the Rx, the achievable rate is maximized as observed in Fig. 3.5(b). Moreover, when the RIS is placed very close to the Rx around 2-3 meters in y-axis, the effective areas of the RIS elements decreases significantly due to the elevation difference between the RIS and Rx. Therefore, the achievable rate is increasing for 2-3 meters as the RIS moves away in the y-axis as seen in Fig. 3.5(b). It should be noted that an improved performance in achievable rate is obtained when the near-field conditions are considered for large RISs.

3.2 Correlation Analysis of the RIS-assisted Channels in mmWave Bands

In this chapter we analyze the spatial correlation between two arbitrary RIS elements by using the simRIS channel simulator [Basar and Yildirim, 2020]. The channels and channel generation procedures are explained in detail in [Basar et al., 2021]. All channel parameters and coefficients are investigated and simulated through simRIS channel simulator [Basar and Yildirim, 2020]. simRIS channel simulator introduce a fundamental channel model by using power scaling laws for RIS-assisted systems in the presence of multiple scatterers and formulate a baseline cascaded physical channel model under the far-field assumption. Furthermore, it considers the 5G mmWave channel model with random number of clusters/scatterers and the characteristics of the RIS, and provides a unified narrow-band channel model for RIS-assisted systems in indoor and outdoor environments [Basar et al., 2021]. The channel correlation was analyzed for indoor and outdoor environments by examining the channel between Tx and RIS. We assume that the total number of M IOs are grouped under C clusters, each having S_c sub-rays for $c = 1, \ldots, C$, that is $M = \sum_{c=1}^{C} S_c$. A cluster can be simply defined as a group of sub-rays that share the same spatial and/or temporal characteristics [Hemadeh et al., 2018]. In light of this information, the vector of Tx-RIS channel coefficients $\mathbf{h} \in \mathbb{C}^{N\times 1}$ can be rewritten for a clustered model by considering array responses and path attenuations:

$$\mathbf{h} = \gamma \sum_{c=1}^{C} \sum_{s=1}^{S_c} \beta_{c,s} \sqrt{G_e(\theta_{c,s}^{\text{RIS}}) L_{\text{T-RIS}}}\ \mathbf{a}(\phi_{c,s}^{\text{RIS}}, \theta_{c,s}^{\text{RIS}}) + \mathbf{h}_{\text{LOS}} \tag{3.17}$$

where $\gamma = \sqrt{\frac{1}{\sum_{c=1}^{C} S_c}}$ is a normalization factor, commonly used in clustered channel models [3GP, 2019], $\mathbf{h}_{\text{LOS}}$ is the LOS component to be discussed later, $\beta_{c,s} \sim \mathcal{CN}(0,1)$ and $L_{\text{T-RIS}}$ respectively stand for the complex Gaussian distributed path gain and attenuation associated with the Tx-RIS link, and $G_e(\theta_{c,s}^{\text{RIS}})$ is the rotationally symmetric RIS element pattern [Nayeri et al., 2018b] in the direction of the (c,s)th scatterer. Here, $\mathbf{a}(\phi_{c,s}^{\text{RIS}}, \theta_{c,s}^{\text{RIS}}) \in \mathbb{C}^{N\times 1}$ is the array response vector of the RIS for the considered azimuth and elevation arrival angles (with respect to the RIS broadside) and given as follows for uniformly distributed RIS elements with an

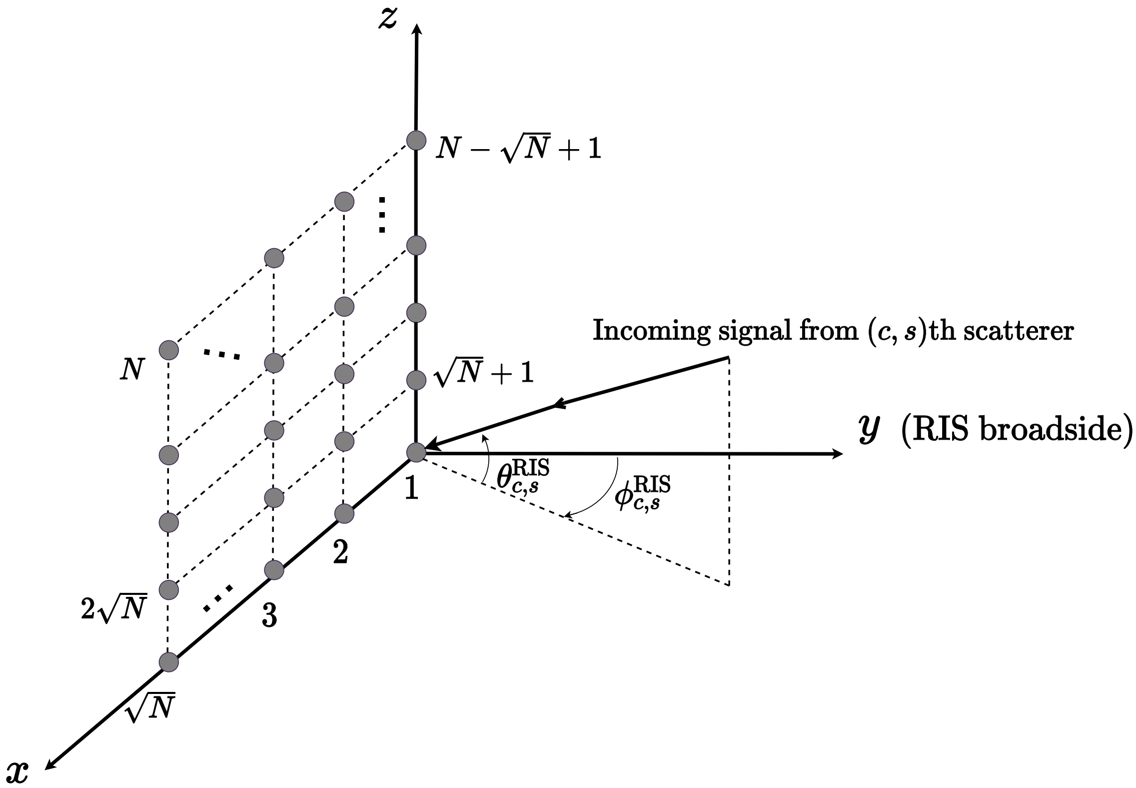

Figure 3.6: 3D array response geometry for a square RIS with N elements.

inter-element spacing of d [Balanis, 2016]:

$$\mathbf{a}(\phi_{c,s}^{\mathrm{RIS}}, \theta_{c,s}^{\mathrm{RIS}}) = \Big[1 \quad \cdots \quad e^{jkd(x \sin\theta_{c,s}^{\mathrm{RIS}} + y \sin\phi_{c,s}^{\mathrm{RIS}} \cos\theta_{c,s}^{\mathrm{RIS}})} \cdots \\ e^{jkd((\sqrt{N}-1)\sin\theta_{c,s}^{\mathrm{RIS}} + (\sqrt{N}-1)\sin\phi_{c,s}^{\mathrm{RIS}}\cos\theta_{c,s}^{\mathrm{RIS}})}\Big]^{\mathrm{T}} \tag{3.18}$$

where $0 \leq x \leq \sqrt{N}-1$ and $0 \leq y \leq \sqrt{N}-1$. To obtain the array response in (3.18), we consider the 3D RIS geometry given in Fig. 3.6, where the RIS elements are counted from right to left and from bottom to up, and the RIS element at the southeast is taken as the reference, that is, corresponds to the first entry of the array response vector.

We analyze the spatial correlation between two arbitrary RIS elements by ignoring the LOS component of the Tx-RIS channel given in (3.17). We assume that all $\theta_{c,s}^{\mathrm{RIS}}$ and $\phi_{c,s}^{\mathrm{RIS}}$ are approximately the same for scatterers within the same cluster.

For simplicity, we assume a square RIS with $\sqrt{N}$ elements at both horizontal and vertical axes while a generalization is straightforward.

Therefore, the elevation and azimuth angles are respectively simplified as θ_c^{RIS} and ϕ_c^{RIS}, where c stands for the index of the corresponding cluster. In order to perform a spatial correlation analysis, since $G_e(\theta_{c,s}^{\text{RIS}})$ and $L_{\text{T-RIS}}$ have relatively small variations, we use the expected value of the term in square root in (3.17) by considering all scatterers in the environment and define it as $\mu = \text{E}\left[\sqrt{G_e(\theta_{c,s}^{\text{RIS}})L_{\text{T-RIS}}}\right]$. A finite number of multipath components is obtained due to the limited number of clusters in the transmission environment, and this leads to a non-isotropic scattering environment. The channel coefficient for the nth element of the RIS can be approximated by

$$h_n \approx \gamma\mu \sum_{c=1}^{C}\sum_{s=1}^{S_c} \beta_{c,s} e^{jkd(n_z \sin(\theta_c^{\text{RIS}}) + n_x \sin(\phi_c^{\text{RIS}})\cos(\theta_c^{\text{RIS}}))} \tag{3.19}$$

where the coordinates of this element are respectively denoted by (n_x, n_z) in horizontal and vertical axes of the RIS by considering the RIS geometry in Fig. 2. The correlation matrix of $\mathbf{h}$ is represented by $\mathbf{R}$, therefore, the correlation coefficient of nth and mth element of the RIS is calculated by

$$\mathbf{R}_{n,m} = \frac{1}{A}\text{E}[h_n h_m^*] = \frac{1}{A}\text{E}\Big[\sum_{i=1}^{C}\sum_{j=1}^{C} \bar{\mu}_i \bar{\mu}_j^* \times e^{jkd[n_z \sin(\theta_i^{\text{RIS}}) - m_z \sin(\theta_j^{\text{RIS}})]\times} \\ e^{jkd[n_x \sin(\phi_i^{\text{RIS}})\cos(\theta_i^{\text{RIS}}) - m_x \sin(\phi_j^{\text{RIS}})\cos(\theta_j^{\text{RIS}})]}\Big] \tag{3.20}$$

where A denotes the normalization coefficient and $\bar{\mu}_c = \gamma\,\mu(\beta_{c,1} + \cdots + \beta_{c,S_c})$ for $c \in \{1, \ldots, C\}$. Since $\beta_{c,s}$ are i.i.d. normal random variables, $\text{E}[\bar{\mu}_i \bar{\mu}_j^*] = 0$ for $i \neq j$. Considering that nth and mth elements of the RIS are located in the same row and $\text{E}[|\bar{\mu}_c|^2] = \gamma^2\mu^2 S_c$ for $c \in \{1, \ldots, C\}$, (3.20) is simplified as

$$\mathbf{R}_{n,m} = \frac{1}{A}\gamma^2\mu^2 \sum_{c=1}^{C} S_c \text{E}\left[e^{jkd_{n,m}\sin(\theta_c^{\text{RIS}})}\right] \tag{3.21}$$

where $d_{n,m}$ represents the distance between nth and mth reflecting elements. If these reflecting elements are not located in the same row, it can be assumed that the coordinate system of the RIS is rotated such that nth and mth reflecting elements are aligned in the same row and the distance between them becomes the horizontal distance as in [Björnson and Sanguinetti, 2020]. Since it is hard to obtain the individual θ_c^{RIS} distribution for each cluster, θ_c^{RIS} should be modeled as the same

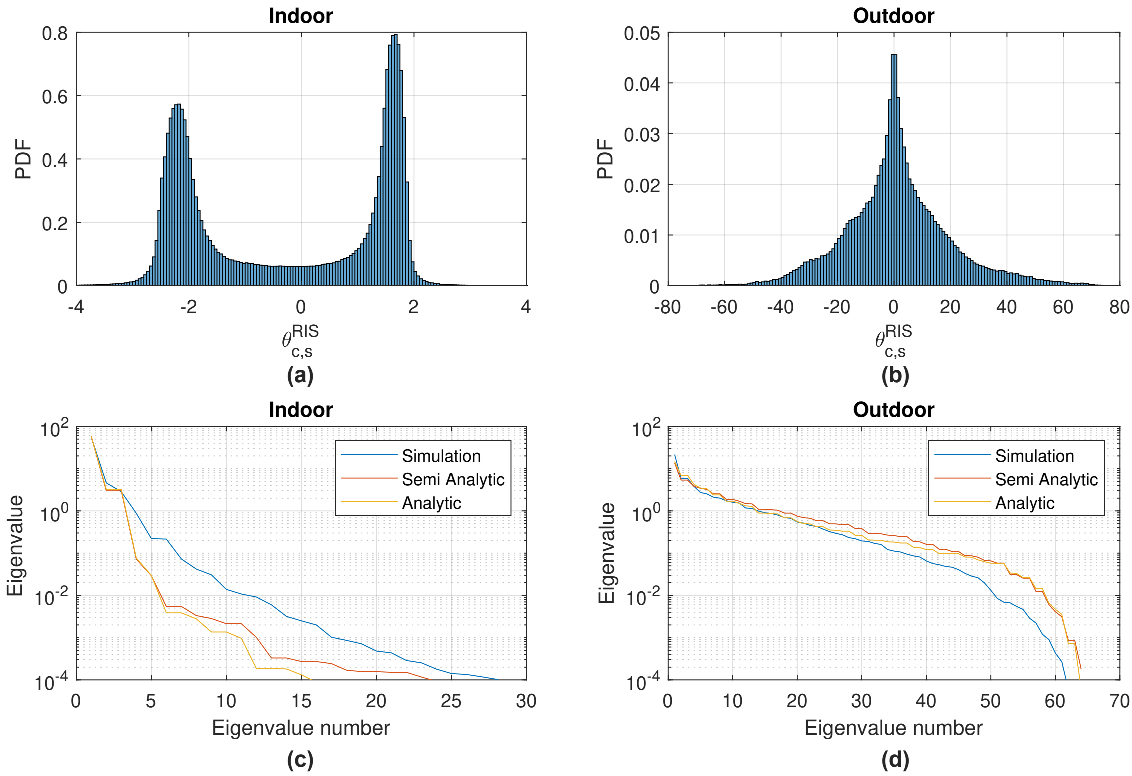

Figure 3.7: The PDF of $(\theta^{\text{RIS}}_{c,s})$ in an (a) indoor and (b) outdoor environment. Eigenvalue spread of spatial correlation matrix in an (c) indoor and (d) outdoor environment.

for all c. Since γ is also a normalization term based on the number of scatterers as expressed in (2), we assume the normalization constant $A = \mu^2$, so that $\mathbf{R}_{n,m} = 1$ for $n = m$. Thus, considering the same distribution for all θ^{RIS}_c in (16), the correlation coefficient between two reflecting elements is represented as follows

$$\mathbf{R}_{n,m} = \mathrm{E}[e^{jkd_{n,m}\sin(\theta^{\text{RIS}}_c)}]. \tag{3.22}$$

Here, the distribution of θ^{RIS}_c depends on the Tx and RIS locations, and the constraints in considered transmission environment. Therefore, it is reasonable to obtain a distribution by considering a large number of θ^{RIS}_c samples for fixed positions of Tx and RIS. Since it is difficult to express the distribution of θ^{RIS}_c mathematically regardless of the Tx and the RIS positions, the correlation coefficient between nth and mth elements can be obtained semi-analytically by taking the mean of many samples from the distribution of θ^{RIS}_c as given below.

$$\mathbf{R}^{s}_{n,m} = \frac{1}{N_\theta}\sum_{i=1}^{N_\theta} e^{jkd_{n,m}\sin(\theta_i^{\text{RIS}})} \tag{3.23}$$

where N_θ represents the number of samples and θ_i^{RIS} is ith sample from the distribution of θ_c^{RIS}.

To get further insights, we obtain the probability density functions (PDFs) of $\theta_{c,s}^{\text{RIS}}$ for indoor and outdoor environments by performing Monte Carlo simulations via SimRIS Channel Simulator as shown in Figs. 3.7(a) and (b) for $N = 64$. Here, the Tx and the RIS are respectively located at $(0, 25, 2)$ and $(40, 50, 2)$ for an indoor environment, while $(0, 25, 40)$ and $(70, 85, 40)$ for an outdoor environment. Since we assume that $\theta_{c,s}^{\text{RIS}}$ is the same for all scatterers within the same cluster, the distribution of θ_c^{RIS} is assumed as the same with $\theta_{c,s}^{\text{RIS}}$. Based on this assumption, we can approximately express the PDFs of θ_c^{RIS} for outdoor and indoor environments, respectively, as follows:

$$f_\theta(\theta_c^{\text{RIS}}) = \frac{1}{22} e^{\frac{-|\theta_c^{\text{RIS}}|}{11}}, -\Delta\theta \leq \theta_c^{\text{RIS}} \leq \Delta\theta, \tag{3.24}$$

$$f_\theta(\theta_c^{\text{RIS}}) = \begin{cases} \frac{2.5}{1.7/0.7} e^{-(\theta_c^{\text{RIS}}+2.3)2.5\,\xi(0.7)^{\xi}}, & 0 < \theta_c^{\text{RIS}} \leq \Delta\theta \\ \frac{3.5}{2.4/1.4} e^{-(\theta_c^{\text{RIS}}-1.7)3.5\xi(1.4)^{\xi}}, & -\Delta\theta \leq \theta_c^{\text{RIS}} \leq 0 \end{cases}. \tag{3.25}$$

In (3.24), θ_c^{RIS} follows a Laplacian distribution with zero-mean and 11^o standard deviation (angular spread) as $\theta_c^{\text{RIS}} \sim \mathcal{L}(0, 11)$ for outdoors, since it depends on $\theta_{c,s}^{\text{Tx}}$ which is a Laplacian distributed random variable as well. Unlike outdoors, the clusters are relatively restricted between the ground and ceiling of the indoor environment, and accumulated in narrow regions. Therefore, $\theta_{c,s}^{\text{RIS}}$ has a very narrow range as seen in Fig. 3.7(a) due to the geometry of the indoor office. In an indoor environment, the distribution of θ_c^{RIS}, with $\Delta\theta$ being the boundary of two different distributions as seen from (3.25), can be modeled by asymmetric Laplacian distribution as $\theta_c^{\text{RIS}} \sim \mathcal{AL}(\tau, \epsilon, \zeta)$, where τ, ϵ and ζ stand for the location, scale and asymmetry parameters, respectively. Moreover, the distribution for indoors is approximated as a pairwise function, $\theta_c^{\text{RIS}} \sim \mathcal{AL}(-2.3, 2.5, 0.7)$ for $0 < \theta_c^{\text{RIS}} \leq \Delta\theta$ and

The PDFs in (3.24) and (3.25) are only used for modeling assumed distribution of θ_c^{RIS} according to Figs. 3.7(a) and 3.7(b).

$\theta_c^{\text{RIS}} \sim \mathcal{AL}(1.7, 3.5, 1.4)$ for $-\Delta\theta \leq \theta_c^{\text{RIS}} \leq 0$ as in (3.25), where $\xi = \text{sign}(\theta_c^{\text{RIS}} - \tau)$. By using the approximated distribution functions in (3.24) and (3.25), the correlation coefficient between two reflecting elements can be derived analytically as follows

$$\mathbf{R}_{n,m}^{a} = \int_{-\Delta\theta}^{+\Delta\theta} e^{jkd_{n,m}\sin(\theta_c^{\text{RIS}})} f_\theta(\theta_c^{\text{RIS}}) d\theta_c^{\text{RIS}}. \tag{3.26}$$

In Figs. 3.7(c) and (d), we investigate the eigenvalue spread of $\mathbf{R}$ by considering the $\theta_{c,s}^{\text{RIS}}$ distributions given in Figs. 3.7(a) and (b), respectively. Eigenvalue spread demonstrates a measure of the spatial correlation as well as the rank of $\mathbf{R}$. For correlated channels, non-identical eigenvalues and a low rank are obtained for $\mathbf{R}$. In an indoor environment, since the number of strong eigenvalues are small, highly correlated channels are obtained due to the narrow range of $\theta_{c,s}^{\text{RIS}}$. Meanwhile, smaller correlation coefficients are obtained in the outdoor environment, since the eigenvalues are relatively distributed equally owing to the larger spread of the scatterers.

Semi-analytical and analytical results are generally in agreement with simulations, while they do not exactly match with the simulation result for increasing eigenvalue numbers, since the approximations for $\theta_{c,s}^{\text{RIS}}$ cause small deviations for higher eigenvalue numbers in distribution as shown in Figs. 3.7(c) and (d). Nevertheless, the analytical and semi-analytical approaches give a useful insight for the characteristics of spatial correlation and motivates us to search for RIS setups with reduced channel correlation.

Chapter 4

RIS-ASSISTED COOPERATIVE NETWORKS

In this chapter, there are two different sections that deal with the integration of RISs into existing technologies. Section 4.1 presents a scheme that utilizes the RIS for NOMA technology and proposes an RIS assisted GF-NOMA scheme. Section 4.2 presents hybrid use cases of RISs with DF-Relays and proposes two different transmission schemes where RISs and relays are operates together.

4.1 RIS-Assisted Grant-Free NOMA

This section focuses on an RIS-aided GF-NOMA scheme where power reception disparity is ensured utilizing novel algorithms dealing with UE clustering, RIS assignment, and RIS phase shift alignment, considering a network consisting of a specific number of users and RISs distributed randomly over the cell coverage area as depicted in Fig. 4.1, where RIS blocks deployed on building facades/windows are highlighted in various colors [Tasci et al., 2022, Kılınç et al., 2022].

Throughout the section, sets and their cardinality are denoted with calligraphic and regular uppercase letters (e.g., $|\mathcal{A}| = A$), respectively. Vectors and matrices are represented in lowercase and uppercase boldfaces (e.g., $\mathbf{a}$ and $\mathbf{A}$), respectively. The i^{th} member of a vector and set is denoted by a_i and $\mathcal{A}\{i\}$, respectively. Likewise, matrix $\mathcal{A}$'s entry on i^{th} row and j^{th} column is denoted by $\mathcal{A}[i, j]$. Subscripts b, r and u are used for indexing the RIS blocks, RB/cluster, and UEs, respectively.

4.1.1 System Model

In this section, we introduce the considered system model in three subsections. In subsection 4.1.1.1, the architecture of the network is demonstrated by addressing the UE distribution as well as RIS deployment and partitioning. In subsection

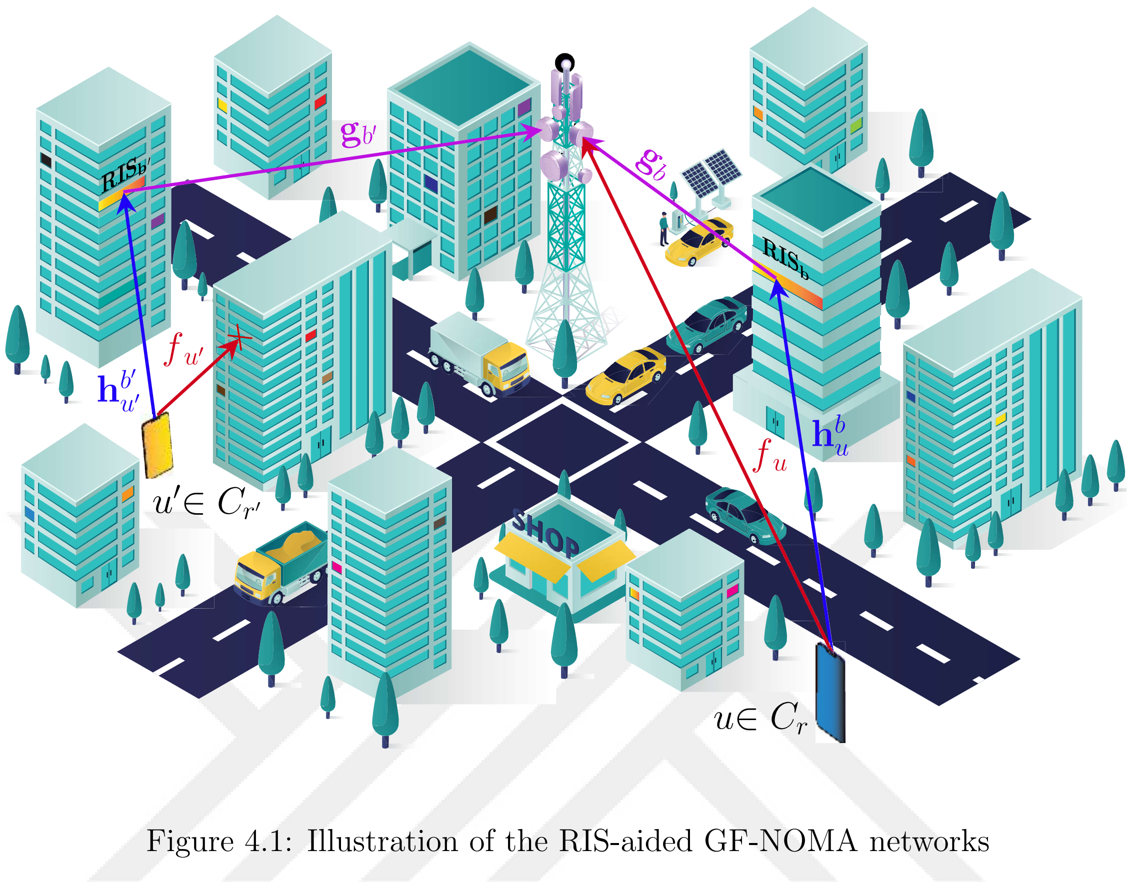

Figure 4.1: Illustration of the RIS-aided GF-NOMA networks

4.1.1.2, the channel model is exhibited in detail. The signal model and SINR of the RIS-assisted scheme is given in the subsection 4.1.1.3.

4.1.1.1 Network Model

We consider UL operation of a network consisting of a single BS serving U UEs over R RBs with W [Hz] bandwidth, whose sets are denoted by $\mathcal{U}$ and $\mathcal{R}$, respectively. All UEs operate at an identical power, p_{id}, which is broadcast by the BS over a control channel. Without loss of generality, UEs are assumed to be uniformly distributed over a cell area of radius D. To show the proposed GF-NOMA schemes' suitability for massive connectivity, we consider a dense network scenario (i.e., $U \gg R$) and group/cluster multiple UEs to utilize a single RB. That is, the number of clusters C is the same with R, and RB/cluster terms are used interchangeably throughout the chapter. Even though R and C are fixed, U can dynamically change according to spatio-temporal characteristics of the network traffic. Hence, the UE density dependent maximum cluster size is set as $K = \lceil \frac{U}{R} \rceil$. Accordingly, the cluster set utilizing RB_r is defined by $\mathcal{C}_r = \{\text{UE}_u \mid \chi_r^u = 1, \forall u \in \mathcal{U}, \sum_{u \in \mathcal{U}} \chi_r^u \leq K\}$, where χ_r^u is the binary UE clustering indicator, i.e., $\chi_r^u = 1$ if UE_u belongs to rth cluster, otherwise $\chi_r^u = 0$.

In order to improve network performance and facilitate the GF-NOMA, M RISs are uniformly deployed in a disk having inner and outer radius of D_{in} and D_{out}, $D_{\text{in}} \leq D_{\text{out}} \leq D$, where D_{in} ensures that RISs are placed at the far-field of the BS as shown in Fig. 4.2. Each physical RIS is partitioned into G logical sub-blocks, each with N elements, resulting in an overall $B = MG$ RIS blocks. Each block can be exploited by a member of a cluster, and a cluster cannot be assigned to more than one block. Accordingly, the set of RIS blocks is denoted by $\mathcal{B}$, and the bth RIS block is denoted by RIS_b. The binary RIS assignment matrix is denoted by $\mathbf{\Delta} \in \{0,1\}^{B \times U \times R}$ with entries $\delta_{r,b}^u$ such that $\delta_{r,b}^u = 1$ if RIS_b is assigned to the rth cluster and configured based on the channels of $\text{UE}_u \in \mathcal{C}_r$, $\delta_{r,b}^u = 0$ otherwise. Fig. 4.1 demonstrates the RIS assignment and phase shift alignment for two different type of UEs. Even though $\text{UE}_u \in \mathcal{C}_r$ has a LoS link to the BS, RIS_b is aligned to its channel to further improve the sum rate of $\mathcal{C}_r$. On the other hand, $\text{RIS}_{b'}$ is aligned to provide coverage to $\text{UE}_{u'} \in \mathcal{C}_{r'}$, whose LoS link to the BS is blocked by a building.

4.1.1.2 Channel Model

The channels are modeled according to the Urban Macro (UMa) scenario of the 3GPP standard specified for 0.5-100 GHz bands [3GP, 2019]. The channel between UE_u and RIS_b is denoted by $\mathbf{h}_u^b = \left[h_{u,b}^1, \ldots, h_{u,b}^n, \ldots, h_{u,b}^N\right] \in \mathbb{C}^{N \times 1}$, where $h_{u,b}^n$ is the channel coefficient from UE_u to nth reflecting element of the RIS_b, $n \in [1, N]$. Similarly, the channel vector between the BS and RIS_b is denoted by $\mathbf{g}_b = \left[g_b^1, \ldots, g_b^n, \ldots, g_b^N\right] \in \mathbb{C}^{N \times 1}$, where g_b^n is the channel coefficient between the BS and nth reflecting element of the RIS_b, $n \in [1, N]$. Moreover, the direct channel from UE_u to the BS is denoted by $f_u \in \mathbb{C}$. All these channels are assumed to experience Rayleigh and Rician fading under line-of-sight (LoS) and non-line-of-sight (NLoS) conditions, respectively. The channel coefficients are modeled as

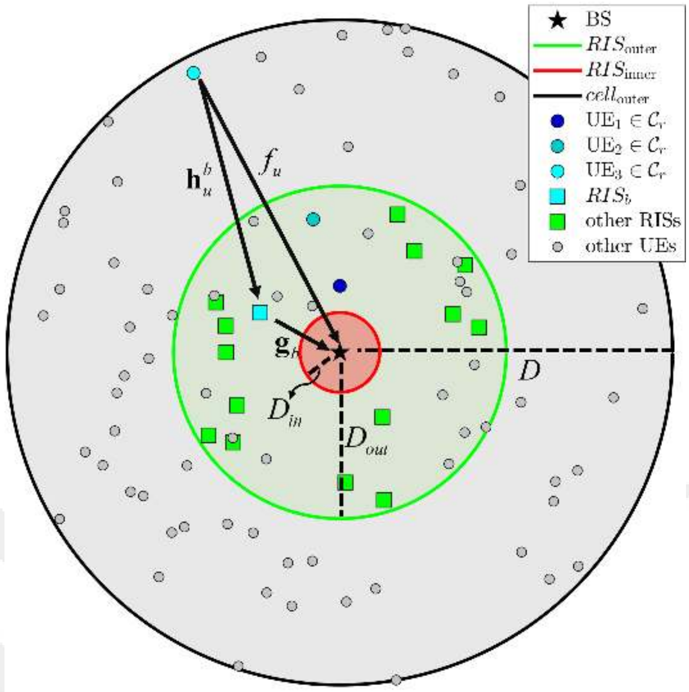

Figure 4.2: Outer and inner cells of the network

$$h_{u,b}^{n} = \sqrt{\frac{1}{\lambda_h}} \left(\sqrt{\frac{K_h}{K_h+1}} h_{u,b}^{n,\mathrm{LoS}} + \sqrt{\frac{1}{K_h+1}} h_{u,b}^{n,\mathrm{NLoS}} \right), \tag{4.1}$$

$$g_{b}^{n} = \sqrt{\frac{1}{\lambda_g}} \left(\sqrt{\frac{K_g}{K_g+1}} g_{b}^{n,\mathrm{LoS}} + \sqrt{\frac{1}{K_g+1}} g_{b}^{n,\mathrm{NLoS}} \right), \tag{4.2}$$

$$f_{u} = \sqrt{\frac{1}{\lambda_f}} \left(\sqrt{\frac{K_f}{K_f+1}} f_{u}^{\mathrm{LoS}} + \sqrt{\frac{1}{K_f+1}} f_{u}^{\mathrm{NLoS}} \right), \tag{4.3}$$

where $K_h/K_g/K_f$ is the Rician factor for $\mathbf{h}_u^b/\mathbf{g}_b/f_u$; $\lambda_h/\lambda_g/\lambda_f$ is the path loss over $\mathbf{h}_u^b/\mathbf{g}_b/f_u$; $h_{u,b}^{n,\mathrm{LoS}}/g_b^{n,\mathrm{LoS}}/f_u^{\mathrm{LoS}}$ is the LoS component; and $h_{u,b}^{n,\mathrm{NLoS}}/g_b^{n,\mathrm{NLoS}}/ f_u^{\mathrm{NLoS}} \sim \mathcal{CN}(0,1)$ is the NLoS component of $\mathbf{h}_u^b/\mathbf{g}_b/f_u$. If a channel does not include a LoS component, which mostly refers to Rayleigh fading, we consider the corresponding Rician factor as 0. λ_h, λ_g, and λ_f can be calculated as per LoS or NLoS links depending on the LoS probability given in [3GP, 2019, Table 7.2-2]. Additionally, the path loss models and the Rician factors are calculated and obtained according to the UMa scenario of the 3GPP standard [3GP, 2019, Table 7.2-1].

4.1.1.3 RIS-Assisted NOMA System

Based on UE-RIS-BS cascaded channels and UE-BS channels defined in the previous subsection, the received complex baseband signal of the proposed system at the BS over RB_r when passive RISs are used can be expressed as

$$y_{r_{\text{pas}}}(\boldsymbol{\Delta}) = \sqrt{p_{\text{id}}} \left(\sum_{\forall u \in \mathcal{C}_r} \sum_{\forall k,l,m} \underbrace{\mathbf{g}_l^{\text{T}} \left(\boldsymbol{\Phi}_{k,l}^m \delta_{k,l}^m \right) \mathbf{h}_u^l s_u}_{\text{UEs-RIS-BS}} + \underbrace{f_u s_u}_{\text{UEs-BS}} \right) + n, \tag{4.4}$$

where $k \in \mathcal{R}$; $l \in \mathcal{B}$; $m \in \mathcal{U}$; $y_{r_{\text{pas}}}(\boldsymbol{\Delta})$ is the received signal from members of $\mathcal{C}_r$ at RB_r; s_u is the symbol transmitted by $\text{UE}_u \in \mathcal{C}_r$; $n \sim \mathcal{CN}(0, \sigma_{\text{Rx}}^2)$ is the additive white Gaussian noise with variance $\sigma_{\text{Rx}}^2 = N_0 W$; N_0 is the thermal noise power spectral density; $\boldsymbol{\Phi}_{k,l}^m = \text{diag}\left(\left[\phi_{k,l}^{m,1}, \ldots, \phi_{k,l}^{m,n}, \ldots, \phi_{k,l}^{m,N} \right] \right) \in \mathbb{C}^{N \times N}$ is the phase shift matrix of RIS_l assigned to $\text{UE}_m \in \mathcal{C}_k$; and $\phi_{k,l}^{m,n}$ is the phase shift of the nth element of the RIS_l configured as per $\text{UE}_m \in \mathcal{C}_k$. Assuming the CSI is acquired through accurate channel estimation methods [Abdallah et al.,] and $\delta_{k,l}^m = 1$, the phase shifts of RIS_b are configured as per the channel characteristics of $\text{UE}_m \in \mathcal{C}_k$

$$\phi_{k,l}^{m,n} = e^{j\angle f_m} e^{-j\angle g_l^n} e^{-j\angle h_{m,l}^n}, \tag{4.5}$$

where $\angle\cdot$ denotes the phase of complex numbers. Element phases cancel the overall channel phases incurred from UE-RIS-BS cascaded channel and UE-BS direct channel.

The SIC receiver at the BS iteratively decodes $y_{r_{\text{pas}}}(\boldsymbol{\Delta})$ in the descending order of received signal power. That is, the cluster member with the strongest/weakest reception power is decoded first/last such that the strongest/weakest cluster member observes all/no intra-cluster interference from other cluster members. Correspondingly, $\widetilde{\mathcal{C}}_r$ denotes the cluster set when the index set of the UEs is sorted in descending order according to the received signal power of the UEs. Accordingly, following from (4.4), the SINR of ith ordered $\mathrm{UE}_u \in \widetilde{\mathcal{C}}_r$ is given by

$$\gamma^{u}_{r_{\mathrm{pas}}}(\boldsymbol{\Delta}) = \frac{p_{\mathrm{id}}\left(\sum\limits_{\forall k,l,m}\left|\mathbf{g}_l^{\mathrm{T}}\left(\boldsymbol{\Phi}^{m}_{k,l}\delta^{m}_{k,l}\right)\mathbf{h}^{l}_{u}\right|^2 + |f_u|^2\right)}{p_{\mathrm{id}}\left(\sum\limits_{\substack{\forall z\in\widetilde{\mathcal{C}}_r[j>i],\\ \forall k,l,m}}\left|\mathbf{g}_l^{\mathrm{T}}\left(\boldsymbol{\Phi}^{m}_{k,l}\delta^{m}_{k,l}\right)\mathbf{h}^{l}_{z}\right|^2 + |f_z|^2\right) + \sigma^2_{\mathrm{Rx}}}, \tag{4.6}$$

where j corresponds to the index of the UEs with lower received signal power than ith ordered cluster member. Even though the SINR expression in (4.6) accounts for $s_u, \forall u \in \mathcal{C}_r$ reflected from $\mathrm{RIS}_b, \forall b \in \mathcal{B}$, regardless of their assignment, the non-coherent signals reflected from RIS blocks assigned to other clusters have a negligible impact on the received signal from $\mathcal{C}_r$, $y_r(\boldsymbol{\Delta})$. Accordingly, (4.6) can be simplified by merely considering the signal reflected from RIS_b assigned to $\mathcal{C}_r$ as follows:

$$\gamma^{u}_{r_{\mathrm{pas}}}(\boldsymbol{\Delta}) = \frac{p_{\mathrm{id}}\left(\sum\limits_{\forall m}\left|\mathbf{g}_b^{\mathrm{T}}\left(\boldsymbol{\Phi}^{m}_{r,b}\delta^{m}_{r,b}\right)\mathbf{h}^{b}_{u}\right|^2 + |f_u|^2\right)}{p_{\mathrm{id}}\left(\sum\limits_{\substack{\forall z\in\widetilde{\mathcal{C}}_r[j>i],\\ \forall m}}\left|\mathbf{g}_b^{\mathrm{T}}\left(\boldsymbol{\Phi}^{m}_{r,b}\delta^{m}_{r,b}\right)\mathbf{h}^{b}_{z}\right|^2 + |f_z|^2\right) + \sigma^2_{\mathrm{Rx}}}. \tag{4.7}$$

4.1.2 Problem Definition and Solution Methodology

In this section, we first provide joint UE clustering and RIS assignment formulation of the RIS-assisted GF-NOMA system, and then provide an overview of the solution methodology.

4.1.2.1 Problem Definition

The joint UE clustering and RIS assignment problem that maximizes the overall network sum rate can be formulated as follows:

$$
\begin{aligned}
\mathbf{P_1} : \max_{\boldsymbol{\mathcal{X}},\boldsymbol{\Delta}} \quad & \sum_{\forall r\in\mathcal{R}}\sum_{\forall u\in\mathcal{U}} W\log_2(1+\chi_r^u\gamma_r^u(\boldsymbol{\Delta})) \\
\text{s.t.} \quad & \\
\mathrm{C}_1: \quad & \gamma_r^u \geq 2^{q_u/B}-1,\ \forall u\in\mathcal{C}_r, \forall r\in\mathcal{R}, \\
\mathrm{C}_2: \quad & \sum_{r\in\mathcal{R}}\chi_r^u = 1,\ \forall u\in\mathcal{U}, \\
\mathrm{C}_3: \quad & \sum_{\forall u\in\mathcal{U}}\chi_r^u \leq K, \quad \forall r\in\mathcal{R}, \\
\mathrm{C}_4: \quad & \delta_{r,b}^u \leq \chi_r^u, \quad \forall r\in\mathcal{R}, \forall b\in\mathcal{B}, \forall u\in\mathcal{U}, \\
\mathrm{C}_5: \quad & \sum_{\forall u\in\mathcal{U}}\sum_{\forall b\in\mathcal{B}}\chi_r^u\delta_{r,b}^u \leq 1, \quad \forall r\in\mathcal{R}, \\
\mathrm{C}_6: \quad & \sum_{\forall u\in\mathcal{U}}\sum_{\forall r\in\mathcal{R}}\sum_{\forall b\in\mathcal{B}}\delta_{r,b}^u \leq B, \\
\mathrm{C}_7: \quad & \chi_r^u\in\{0,1\}, \delta_{r,b}^u\in\{0,1\}, \forall r, \forall u, \forall b,
\end{aligned}
\tag{4.8}
$$

where γ_r^u is the SINR of $\mathrm{UE}_u \in \mathcal{C}_r$, $\boldsymbol{\mathcal{X}} \in \{0,1\}^{U\times R}$ is the binary UE clustering matrix with entries χ_r^u. In $\boldsymbol{P_1}$, C_1 ensures that UE_u is satisfied with the quality of service demand q_u [bps] $\forall u \in \mathcal{C}_r, \forall r \in \mathcal{R}$, C_2 assures each UE is admitted to a cluster, C_3 limits the cluster size by $K = \lceil U/R \rceil$, C_4 states that RIS_b cannot be configured as per UE_u if it is not a member of $\mathcal{C}_r$, C_5 guarantees each cluster is assisted by at most one RIS block, C_6 limits the total RIS assignments by the total number of RIS blocks, and C_7 specifies the domain and bounds on optimization variables. $\mathbf{P_1}$ is a mixed-integer non-linear programming (MINLP) problem, which is non-convex due to the interference terms in the SINR expression defined in the next section. Finding an optimal solution to this NP-Hard problem is computationally prohibitive, even for moderate network size, and it necessitates a heuristic solution for real-life implementation, which is discussed next.

4.1.2.2 Solution Methodology

The proposed RIS-assisted GF-NOMA scheme allows UEs to access RBs at any time, requiring neither grant acquisition from the BS nor power control at the UE side. Instead, the power disparity requirement of PD-NOMA is satisfied by the UE clustering and the RIS assignment through a three-level implicit power control:

1. The first level of power control is obtained by pairing UEs with different channel gains on the same cluster/RB. Even if UEs operate at identical transmit power, the channel gain disparity introduces a reception power disparity to achieve a higher PD-NOMA gain.

2. The second level of power control is obtained by assigning a proper RIS block to a cluster. It is worth noting that RIS improves overall communication performance if it is deployed near the UE or the BS [Kilinc et al., 2021]. Therefore, RIS block assignment plays a crucial role in increasing the power reception disparity for an improved cluster sum rate.

3. The final level of power control is obtained by selecting the cluster member according to which assigned RIS is configured. Since reception power levels determine the SIC decoding order, the cluster member selection is also critical for improving the overall cluster sum rate.

Before delving into the details of the proposed UE clustering and RIS assignment solutions for the considered RIS-assisted GF-NOMA system, it is worth reminding that the optimal GB PD-NOMA scheme requires UEs with stronger channels to transmit at the higher powers to maximize the UL-NOMA cluster sum rate [Celik, 2021]. However, this approach is not fair in energy consumption and may result in reduced network lifetime, which is paramount for low-power mMTC. Alternatively, the proposed approaches improve network lifetime by requiring all UEs to transmit at identical power fairly and constitutes the required power disparity through iterative UE clustering and RIS assignments introduced in Section 4.1.3.

Algorithm 1 : Joint UE Clustering and RIS Assignment

Input: $\mathcal{R}, \mathcal{U}, \mathcal{B}$, P
$\mathbf{h}_u^b/\mathbf{g}_b/f_u \leftarrow$ *Acquire CSI from SRS sent by* $UE_u, \forall u \in \mathcal{U}, \forall b \in \mathcal{B}$
$C \leftarrow R$ *// Determine number of clusters*
$K \leftarrow \left\lceil \frac{U}{R} \right\rceil$ *// Determine maximum cluster size*
$\tilde{\mathcal{U}} \leftarrow \textsc{SortDescend}(\mathfrak{Rss}, \forall u)$ *// UE ordering based on RSS of SRS signals*
$\mathcal{C}_r \leftarrow \tilde{\mathcal{U}}\{r\}, r \in [1, \ldots, R]$ *// Initialize clusters*
$\chi_r^u \leftarrow 1, u \in \mathcal{C}_r$ *//Initialize UE clustering matrix*
for $k = 1 : K-1$ **do** *// Iterative UE admission and RIS Assignment starts*
  $\mathcal{A}_k \leftarrow \tilde{\mathcal{U}} - \bigcup_{r=1}^{R} \mathcal{C}_r$ *// Initialize admission awaiting UEs*
  $\boldsymbol{Q_k}, \boldsymbol{I_k} \leftarrow \textsc{Cost Matrix}(\boldsymbol{C}_r, \mathcal{A}_k, \mathcal{B})$ *// Generating cost matrix*
  $\boldsymbol{Y}_k \leftarrow \textsc{3D-Axial Assignment}(\boldsymbol{Q_k}, \mathcal{A}_k)$
  $\mathcal{C}_r \leftarrow \mathcal{C}_r \bigcup \mathcal{A}_k\{u\}, y_{r,b}^u = 1, \forall (r, u, b)$ *// Update clusters*
  $\chi_r^u \leftarrow 1, u \in \mathcal{C}_r$ *// Update UE clustering matrix*
  $\delta_{r,b}^{u'} \leftarrow 1$ iff $u' = \iota_{r,b}^u$, $u \in \mathcal{C}_r, \forall (r, b)$ *//Update RIS assignment matrix*
end for
return $\boldsymbol{\mathcal{X}}, \boldsymbol{\Delta}$

procedure $\textsc{Cost Matrix}(\boldsymbol{C}_r, \mathcal{A}_k, \mathcal{B})$
  $\boldsymbol{Q}, \boldsymbol{I} \leftarrow \mathbf{0}^{R \times A \times B}$ *// Initialize* $\boldsymbol{Q}$ *and* $\boldsymbol{I}$ *to matrix of zeros*
  for $r = 1 : \mathcal{R}$ **do**
    for $b = 1 : B$ **do**
      for $u = 1 : A$ **do**
        $\mathcal{T}_r \leftarrow \mathcal{C}_r \bigcup \mathcal{A}_k\{u\}$ *// Temp. admit* u^{th} *UE of* $\mathcal{A}_k$ *to* $\mathcal{C}_r$
        for $j \in T_r$ **do**
          $\boldsymbol{\Phi}_{r,b}^j \leftarrow$ Align RIS_b to $\text{UE}_{\mathcal{T}_r\{j\}}$ as per (4.5)
          $\gamma_r^j \leftarrow$ Obtain SINR as per (4.7)
          $\eta_j^\star \leftarrow \sum_{j \in \mathcal{T}_r} W \log_2(1 + \gamma_r^j)$
        end for
        $q_{r,b}^u \leftarrow \max(\eta_j^\star, j \in \mathcal{T}_r)$ *// Update cost matrix entries*
        $\iota_{r,b}^u \leftarrow \text{argmax}(\eta_j^\star, j \in \mathcal{T}_r)$ *// Update* $\boldsymbol{I}$ *entries*
      end for
    end for
  end for
return $\boldsymbol{Q}, \boldsymbol{I}$
end procedure

procedure $\textsc{3D-Axial Assignment}(\boldsymbol{Q}, \mathcal{A}_k)$
  $\overset{\star}{\boldsymbol{Y}} \leftarrow \max_{\boldsymbol{Y}} \sum_{r \in \mathcal{R}} \sum_{b \in \mathcal{B}} \sum_{u \in \mathcal{U}} q_{r,b}^u y_{r,b}^u$
    s.t. $\sum_{r \in \mathcal{R}} \sum_{b \in \mathcal{B}} y_{r,b}^u = 1, \forall u \in \mathcal{A}_k$
    $\sum_{r \in \mathcal{R}} \sum_{u \in \mathcal{U}} y_{r,b}^u = 1, \forall b \in \mathcal{B}$
    $\sum_{b \in \mathcal{R}} \sum_{u \in \mathcal{U}} y_{r,b}^u = 1, \forall r \in \mathcal{R}$
return $\overset{\star}{\boldsymbol{Y}}$
end procedure

4.1.3 UE Clustering and RIS Assignment Algorithms

In this section, we introduce the proposed UE clustering and RIS assignment schemes. Following cluster initialization, the proposed iterative approach admits a single UE to each cluster at each iteration until all UEs are admitted to a cluster. To this aim, the admissions are determined based on two different algorithms. Algorithm

1 jointly assigns UEs and RISs to clusters and executes a 3D-AA that yields the maximum network sum rate; therefore, it is called joint UE clustering and RIS assignment algorithm. Algorithm 2 first assigns UEs to clusters by using linear sum assignment (LSA). After that, it assigns RIS blocks to formed clusters by using LSA again. Since the second assignment first forms clusters and then makes RIS assignments, it follows a two-step process, unlike Algorithm 1, which is called consecutive UE clustering and RIS assignment algorithm.

4.1.3.1 Joint 3D UE Clustering and RIS Assignment Algorithm

Algorithm 1 follows an iterative joint 3D assignment approach. At each iteration, a 3D cost matrix is generated whose elements represent cluster rates for each combination of UE admission and RIS assignment status. UEs and RISs are then jointly assigned to clusters using a 3D-AA.

Algorithm 1 starts with receiving sounding reference signals (SRS), which is a Zadoff-Chu sequence transmitted by each UE separately from the Physical UL shared channel (PUSCH) and physical UL control channel (PUCCH). UEs can transmit SRS on any subcarriers in the last symbol of an UL subframe regardless of subcarriers assignments. We especially focus on time-division duplexing (TDD) mode for the sake of channel reciprocity such that SRS may also be sent in the last two symbols of the special subframe if UL pilot time slot (UpPTS) is configured to be in the long format. The SRS is imperative to estimate cascaded and direct channels [Abdallah et al.,] to determine RIS assignment and configure phase shift matrices accordingly. Notice that the CSI acquisition is an inherent part of any communication system and not specific to the proposed approach. After the cluster size is determined based on the available number of RBs in Line 3, the maximum cluster size is determined in Line 4 based on the UE density. For the sake of cluster initialization, the UEs are sorted in the descending order of received signal strength of SRS signals in Line 5. Then, the clusters are initialized by admitting the first R UEs into C clusters in Line 6. Then, the iterative UE admission and RIS assignment starts in Line 8, in each iteration one more UE is admitted to each cluster. Therefore, the first line of the for loop, Line 9, updates the set of UEs awaiting cluster admission, which is denoted by $\mathcal{A}_k$.

To execute 3D-AA, Line 10 calls cost matrix generation procedure given between Line 17 and Line 34, where cost matrix $\boldsymbol{Q} \in \mathbb{R}^{R\times A\times B}$ and temporary RIS alignment matrix $\boldsymbol{I} \in \mathbb{N}^{R\times A\times B}$ are formed over three nested for loops. In Line 22, the u-th element of admission awaiting UE set is temporarily admitted to $\mathcal{C}_r$. Then, the most inner loop between Line 23 and Line 27 determines the cluster member giving the maximum cluster sum rate if RIS_b is aligned as per its channel conditions. To this aim, Line 24 adjusts the phase shift matrix of RIS_b to $\text{UE}_{\mathcal{T}_r\{j\}}$, Line 25 calculates the cluster members' SINR based on adjusted the phase shift matrix as per (4.7), and finally Line 26 records the cluster sum rate of $\mathcal{T}_r$ if RIS_b is aligned to its j-th member, $\eta_j^\star$. Accordingly, the cost matrix element $q_{r,u}^b$ is updated in Line 28 based on the UE cluster member giving the highest possible cluster rate if the phase shift matrix of RIS_b is aligned to itself, whose index matrix (representing the UE index) is also stored in a temporary RIS alignment matrix in Line 29.

Following the generation of the cost-matrix, Line 11 calls 3D-Axial Assignment to find joint UE clustering and RIS assignment at k-th iteration. For instance, when 3D-AA returns $y_{3,4}^5 = 1$, it means that: 1) $\text{UE}_{\mathcal{A}_k\{5\}}$ is admitted to $\mathcal{C}_3$, 2) RIS_4 is assigned to $\mathcal{C}_3$, and 3) phase shift matrix of RIS_4 is aligned to assisted UE whose UE index stored in $u' = \iota_{3,4}^5$. Thereafter, the cluster members are updated as per the outcome of 3D-AA in Line 12, which is followed by update of UE clustering matrix $\boldsymbol{\mathcal{X}}$ and RIS assignment matrix $\boldsymbol{\Delta}$ in Line 13 and 14, respectively. The final UE clustering and RIS assignment matrices are returned at the end of $(K-1)$-th iteration. Notice in Line 14 that the phase alignment is obtained from the RIS alignment matrix $\boldsymbol{I}$ returned by the Cost Matrix procedure.

The time complexity of the proposed solution is mainly driven by Cost Matrix and 3D-Axial Assignment procedures. The complexity of cost matrix computation is $\mathcal{O}\left(\sum_{k=1}^{K-1} RA_kB\right)$. Moreover, the 3D-AA is known to be an NP-Hard problem, whose matching theory-based approximate solutions can obtain results for a square cost matrix with complexity $\mathcal{O}\left(3MV^3\right)$ where M is the number of relaxations and V is the largest dimension of the cost matrix [Pattipati et al., 1992].

Hence, after $K-1$ iterations, the time complexity of the considered 3D-AA becomes $\mathcal{O}\left(3M\sum_{k=1}^{K-1}(V_k)^3\right)$, where $V_k = \max(R, A_k, B)$. Since the latter is more dominant, the overall complexity can be approximated as $\sim \mathcal{O}\left(3M\sum_{k=1}^{K-1} RA_kB + (V_k)^3\right)$.

4.1.3.2 Consecutive 2D UE Clustering and RIS Assignment Algorithm

Algorithm 2 proposes a faster and consecutive UE clustering and RIS assignment algorithm that achieves almost the same performance as Algorithm 1. Algorithm 2 mainly follows a similar iterative clustering approach but instead of jointly assigning UEs and RIS blocks to cluster sets, it first assigns UEs to the clusters and then assigns RISs to previously formed clusters. Lines 2-6 performs setting obtaining CSI information, determining number of clusters and maximum cluster size, initializing clusters respectively, as in Algorithm 1.

The iterative UE admission starts in Line 8, in each iteration one more UE is admitted to each cluster. Therefore, the first line of the for loop, Line 9, updates the set of UEs awaiting cluster admission, which is denoted by $\mathcal{A}_k$. The iterative algorithm now only admits UEs to the clusters and starts in Line 8. In line 9 the set $\mathcal{A}_k$ is updated that denotes the admission awaiting UEs. In each iteration one more UE is admitted to each cluster from the set $\mathcal{A}_k$. Line 10 calls the cost matrix function for UE admission. The 2D Cost matrix $\boldsymbol{Q}_k \in \mathbb{R}^{R\times A}$ is generated between the Lines 20-31 over two nested loops. Line 24 admits the uth UE from the set $\mathcal{A}_k$ to $\mathcal{C}_r$ and forms a temporary cluster denoted by $\mathcal{T}_r$. The UE SINRs are calculated in Line 25 and the temporary cluster rate is calculated by summing the rates of UEs in $\mathcal{T}_r$. The cost matrix element q_r^u in Line 26 stands for the cluster rate if uth UE from the set $\mathcal{A}_k$ is assigned to C_r. Notice that the UE assignment merely depends on channel gain disparity among the UEs and does not consider RIS assistance and phase shift alignment.

The UE admission is performed according to LSA executed in Line 11 to find the assignment maximizing the network sum rate by using the generated cost matrix at kth iteration. For instance, when LSA returns $y_3^5 = 1 \in \boldsymbol{Y}_k$, it means that $\text{UE}_{\mathcal{A}_k\{5\}}$ is admitted to $\mathcal{C}_3$. In the final step, UE clustering matrix $\boldsymbol{\mathcal{X}}$ is updated. After

Algorithm 2 : Consecutive UE Clustering and RIS Assignment

Input: $\mathcal{R}$, $\mathcal{U}$, $\mathcal{B}$, P
$\mathbf{h}_u^b/\mathbf{g}_b/f_u \leftarrow$ *Acquire CSI from SRS sent by* $UE_u, \forall u \in \mathcal{U}, \forall b \in \mathcal{B}$
$C \leftarrow R$ *// Determine number of clusters*
$K \leftarrow \lceil \frac{U}{R} \rceil$ *// Determine maximum cluster size*
$\tilde{\mathcal{U}} \leftarrow$ SortDescend($\mathfrak{Rss}, \forall u$) *// UE ordering based on RSS of SRS signals*
$\mathcal{C}_r \leftarrow \tilde{\mathcal{U}}\{r\}, r \in [1, \ldots, R]$ *// Initialize clusters*
$\chi_r^u \leftarrow 1, u \in \mathcal{C}_r$ *//Initialize UE clustering matrix*
for $k = 1 : K - 1$ **do** *// Iterative UE admission and RIS Assignment starts*
    $\mathcal{A}_k \leftarrow \tilde{\mathcal{U}} - \bigcup_{r=1}^{R} \mathcal{C}_r$ *// Initialize admission awaiting UEs*
    $\boldsymbol{Q_k} \leftarrow$ Cost Matrix UE($\boldsymbol{C}_r, \mathcal{A}_k$) *// CM for user clustering*
    $\boldsymbol{Y}_k \leftarrow$ 2D-Axial Assignment($\boldsymbol{Q_k}$)
    $\mathcal{C}_r \leftarrow \mathcal{C}_r \bigcup \mathcal{A}_k\{u\}, y_r^u = 1, \forall (r, u)$ *// Update clusters*
    $\chi_r^u \leftarrow 1, u \in \mathcal{C}_r$ *// Update UE clustering matrix*
end for
return $\boldsymbol{\mathcal{X}}$
$\boldsymbol{Q_m}, \boldsymbol{I_m} \leftarrow$ Cost Matrix RIS($\boldsymbol{C}_r, \mathcal{B}$) *// CM for RIS assignment*
$\boldsymbol{Y}_m \leftarrow$ 2D-Axial Assignment($\boldsymbol{Q_m}$)
$\delta_{r,b}^{u'} \leftarrow 1$ iff $u' = \iota_r^b, y_r^b = 1, u \in \mathcal{C}_r, \forall (r, b)$ *//Update RIS assignment matrix*
return $\boldsymbol{\Delta}$

---

procedure Cost Matrix UE($\boldsymbol{C}_r, \mathcal{A}_k$)
    $\boldsymbol{Q}, \boldsymbol{I} \leftarrow \mathbf{0}^{R \times A}$ *// Initialize* $\boldsymbol{Q}$ *and* $\boldsymbol{I}$ *to matrix of zeros*
    for $r = 1 : \mathcal{R}$ **do**
        for $u = 1 : A$ **do**
            $\mathcal{T}_r \leftarrow \mathcal{C}_r \bigcup \mathcal{A}_k\{u\}$ *// Temp. admit* u^{th} *UE of* $\mathcal{A}_k$ *to* $\mathcal{C}_r$
            $\gamma_r^j \leftarrow$ Obtain SINR of $\text{UE}_j, \forall j \in \mathcal{T}_r$
            $q_r^u \leftarrow \sum_{j \in \mathcal{T}_r} W \log_2(1 + \gamma_r^j)$
        end for
    end for
return $\boldsymbol{Q}$

end procedure

---

procedure Cost Matrix RIS($\boldsymbol{C}_r, \mathcal{B}$)
    $\boldsymbol{Q}, \boldsymbol{I} \leftarrow \mathbf{0}^{R \times B}$ *// Initialize* $\boldsymbol{Q}$ *and* $\boldsymbol{I}$ *to matrix of zeros*
    for $r = 1 : \mathcal{R}$ **do**
        for $b = 1 : B$ **do**
            for $j \in C_r$ **do**
                $\boldsymbol{\Phi}_{r,b}^j \leftarrow$ Align RIS_b to $\text{UE}_{\mathcal{C}_r\{j\}}$ as per (4.5)
                $\gamma_r^j \leftarrow$ Obtain SINR as per (4.7)
                $\eta_j^\star \leftarrow \sum_{j \in \mathcal{T}_r} W \log_2(1 + \gamma_r^j)$
            end for
            $q_r^b \leftarrow \max(\eta_j^\star, j \in \mathcal{C}_r)$ *// Update cost matrix entries*
            $\iota_r^b \leftarrow \text{argmax}(\eta_j^\star, j \in \mathcal{C}_r)$ *// Update* $\boldsymbol{I}$ *entries*
        end for
    end for
return $\boldsymbol{Q}, \boldsymbol{I}$
end procedure

---

procedure 2D-Axial Assignment($\boldsymbol{Q}$)
    $\overset{\star}{\boldsymbol{Y}} \leftarrow \max_{\boldsymbol{Y}} \sum_{r \in \mathcal{R}} \sum_{z \in \mathcal{Z}} q_r^z y_r^z$
        s.t. $\sum_{r \in \mathcal{R}} y_r^z = 1, \forall z \in \mathcal{Z}$
        $\sum_{z \in \mathcal{Z}} y_r^z = 1, \forall r \in \mathcal{R}$
        $z \in \{u, b\}, \mathcal{Z} \in \{\mathcal{U}, \mathcal{B}\}$
return $\overset{\star}{\boldsymbol{Y}}$
end procedure

finalizing the UE admission and forming clusters, RIS blocks needs to be assigned to generated clusters and assist specific UEs in each cluster to maximize the cluster rate. Line 16 calls the cost matrix function for RIS assignment and phase alignment purposes. The cost matrix $\boldsymbol{Q}_m \in \mathbb{R}^{R\times B}$ and a temporary RIS alignment matrix $\boldsymbol{I}_m \in \mathbb{N}^{R\times B}$ are formed over three nested for loops in procedure explained between lines 32-46. The first two loops in lines 34 and 35 assign $\text{RIS}_b \in \mathcal{B}$ to $\mathcal{C}_r$. The most inner loop finds the UE that maximizes the cluster sum rate when the corresponding RIS block's phase shifts are aligned to itself. Line 37 aligns the phase of the RIS_b to UE $j \in \mathcal{C}_r$. Following SINRs are calculated by considering the phase configuration of the RIS block in Line 38. Line 39 records the cluster sum rate if RIS_b is assigned to UE j in $\mathcal{C}_r$. In consequence, the cost matrix element q_r^u in Line 42 is obtained by considering the cluster member yielding the largest cluster rate when assisted with RIS_b and its UE index is stored in ι_r^b. Finally, LSA procedure is called again in Line 17 to find the RIS assignment and alignment at once. For instance, if LSA returns $y_2^4 = 1 \in \boldsymbol{Y}_k$ for user clustering, it means that RIS_4 is assigned to $\mathcal{C}_2$. Likewise, if LSA returns $y_2^4 = 1 \in \boldsymbol{Y}_m$ for RIS assignment/alignment, it means that the phase configuration of the RIS_4 is aligned for $\text{UE}_{u'}$ whose UE index is stored in ι_2^4. Thereafter, the elements of the RIS assignment matrix $\delta_{r,b}^{u'}$ is updated in Line 18 and returned the final assignment matrix $\boldsymbol{\Delta}$ in 19.

The time complexity of the consecutive approach is mainly driven by Cost Matrix and LSA procedures. The complexity of cost matrix computation for UE clustering and RIS assignment are given by $\mathcal{O}\left(\sum_{k=1}^{K-1} RA_k\right)$ and $\mathcal{O}\left(RB\right)$, respectively. Considering the well known cubic complexity of LSA solutions, the overall complexity can be obtained as $\mathcal{O}\left(\sum_{k=1}^{K-1} RA_k + (\max(R, A_k))^3\right)$ and $\mathcal{O}\left(RB + (\max(R,B))^3\right)$, which constitutes the entire complexity of Algorithm 2 together.

4.1.4 Numerical Results

In this section, we provide numerical results for the proposed schemes and compare their performances with three benchmark schemes for different system parameters.

Table 4.1: TABLE OF THE SIMULATION PARAMETERS

Param.	Def.	Value	Param.	Def.	Value
U	# UEs	75	N	# Reflecting elements	256
R	# RBs	25	q_u	Quality of service demand of UEu	0.1 Mbps
M	# RISs	25	f_c	Carrier frequency	5 GHz
G	# sub-blocks	1	p_{id}	Identical power	21 dBm
C	# clusters	25	$P_{\max}$	Maximum transmit power of the UEs	23 dBm
N_0	Thermal noise power spectral density	−174 dBm	$P_{\min}$	Minimum transmit power of the UEs	−40 dBm
D	Cell radius	250 m	W	Resource block bandwith	180 kHz
D_{in}	RIS area inner radius	15 m	D_{out}	RIS area outer radius	50 m

Achievable rates and fairness indexes for different schemes are presented by computer simulations. Although we consider the SINR expressions in (4.7) for RIS assignment in both algorithms, we consider the general SINR expression in (4.6) while obtaining the numerical results, so that the reflections from non-coherent RIS blocks are considered as well. We consider the default system parameters summarized in Table 4.1, unless stated explicitly otherwise.

4.1.4.1 Benchmark Schemes

For evaluation of the RIS-Assisted GF-NOMA scheme, this section presents three benchmark schemes [Celik, 2021]:

1. The OPT PD-NOMA (OPT PD-NOMA) where UEs compute optimal power control based on the readily available CSI, and the maximum and minimum transmit power of UEs are $P_{\max}$ and $P_{\min}$, respectively. Throughout the simulations, optimal power weights are obtained by geometric programming solver of the CVX disciplinized convex optimization toolbox [Grant and Boyd, 2014].

2. Multi-level GF-NOMA (MGF-NOMA) scheme partitions the set of UEs into $R = C$ groups based on their channel gains and divides power control range ($[p_{max} = 23, p_{min} - 40]$ dBm) into $R = C$ levels. MGF-NOMA requires UE partitions with higher channel gain to transmit at higher power levels. For instance, the UE partition consisting of UEs with the highest/lowest channel

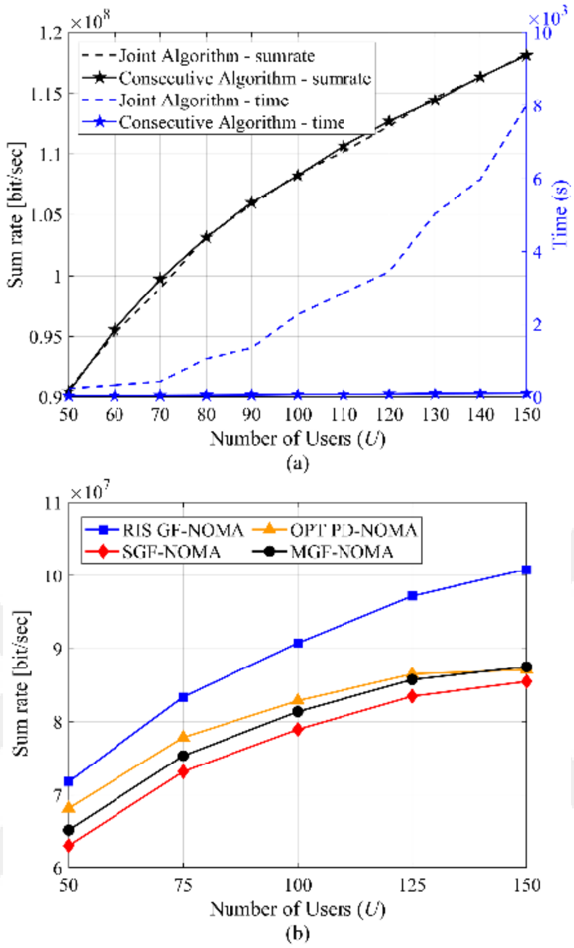

Figure 4.3: (a) Sum rate and complexity of the proposed algorithms, and (b) sum rate of the proposed schemes

gains are required to transmit at the highest/lowest power levels.

3. Single level GF-NOMA (SGF-NOMA) scheme requires all UEs transmit at an identical transmit power, p_{id}.

We refer interested readers to [Celik, 2021] for a more detailed explanation of the benchmark schemes. For the sake of a fair comparison, the benchmark schemes follow the clustering approach presented in Algorithm 2. Additionally, for the same reason, the proposed schemes uses $p_{\text{id}} = 21$ dBm for all UEs, which is the average transmit power of UEs for OPT PD-NOMA. Noting that benchmark schemes do not benefit from RIS, the main difference between compared schemes is the underlying power control approach.

4.1.4.2 Impact of UE Density on Sumrate and Time Complexity

The number of UEs in the network is a crucial metric affecting both network performance and the complexity of the NOMA schemes. Fig. 4.3 shows run time complexity and network achievable network sum rate for varying U. As seen in Fig. 4.3(a), the consecutive algorithm returns result up to 80 times faster than the joint Algorithm 1 while achieving almost the same network sum rate performance as shown in 4.3(b). Such a great run time complexity difference is mainly due to the time spent generating the 3D cost matrix for Algorithm 1, which increases as U increases. Since the consecutive approach provides almost the same performance with much-reduced running times, the rest of the simulations are carried out with Algorithm 2.

As seen in Fig. 4.3(b), the sum rate of the proposed scheme increases with U because the number of UEs operating in a single RB increases, resulting in more efficient spectrum usage. The proposed scheme with RIS performs up to 15%, 15%, and 18% better than OPT PD-NOMA, MGF-NOMA, and SGF-NOMA schemes when $U = 150$, respectively. We note that the increase in the cluster size does not negatively affect the network performance. The proposed scheme performs better on denser networks, where $U = 150$ and the number of UEs per cluster is 6 and outperforms the benchmark schemes. The performance of the benchmark schemes starts to saturate after $U = 150$ while the proposed scheme continues to show an upwards trend.

4.1.4.3 The Impact of Identical Tx Power on Fairness

The network sum rate for varying identical transmit power levels, p_{id}, is presented in Fig. 4.4(a). As the p_{id} varies for SGF-NOMA and RIS-assisted GF-NOMA, transmit power levels are fixed in MGF-NOMA, and the average transmit power between UEs is obtained as 21 dBm for adaptively regulated OPT PD-NOMA via Monte Carlo simulations. While the SGF-NOMA achieves the same performance as MGF-NOMA and OPT GF-NOMA at the maximum transmit power level, the RIS-assisted scheme require less power at the UE side, resulting in more energy-efficient

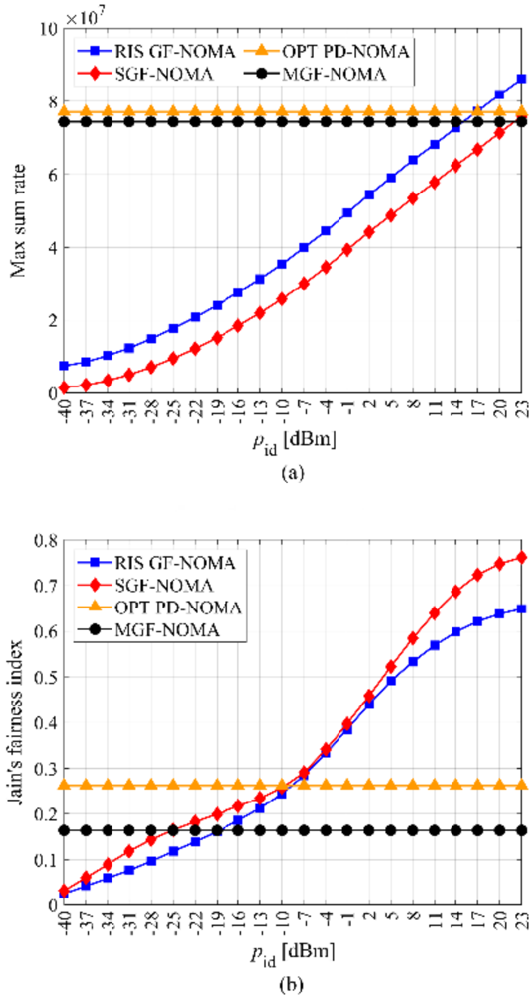

Figure 4.4: Sum rate and Jain's fairness index for varying p_{id} for the proposed and benchmark schemes

transmission. The RIS-assisted scheme requires 4 dB less transmit power to achieve the same performance as OPT PD-NOMA and MGF-NOMA. The evaluation of the fairness in terms of the energy efficiencies of the UEs sharing the same cluster is presented in Fig. 4.4(b). The Jain's fairness index is obtained for each scheme as follows:

$$\mathcal{J} = \frac{\left(\sum_{\forall u \in \mathcal{C}_r} \eta_u\right)^2}{K\left(\sum_{\forall u \in \mathcal{C}_r} \eta_u\right)} \tag{4.9}$$

where $\eta_u = R_u/P_{\text{t}}^u$, R_u, P_{t}^u are the bit per joule energy efficiency, the achievable rate, and transmit power of the UE$_u$, respectively. Since UEs transmit at identical power levels, the SGF-NOMA and RIS-assisted GF-NOMA scheme present higher fairness. The SGF-NOMA and RIS-assisted GF-NOMA perform close fairness results. However, as the transmit power of the UEs increases, achievable rates of the assisted UEs become dominant, resulting in poorer fairness compared to the SGF-NOMA. Looking at Fig. 4.4, it can be concluded that RIS-assisted GF-NOMA schemes maintain fairness among UEs while providing enhanced capacity.

Network sum rate for varying D_{out}, R, and N are presented in Fig. 4.5(a), 4.5(b), and 4.5(c), respectively. As seen in Fig. 4.5(a), the locations of the RISs substantially affect the system performance. It is a well-known fact that a basic RIS-assisted system exhibits its maximum performance when the RIS is located near the system's terminals. Similarly, the proposed design performs best when the RISs are close to the BS or UEs. The results show that deploying RISs near the BS performs better than the uniform deployment of RIS across the cell area. This is mainly because we cannot guarantee that the RISs will be placed close to the UEs since UEs are also randomly distributed. The proposed scheme performs 8%, 12%, and 15% better than OPT PD-NOMA, MGF-NOMA, and SGF-NOMA schemes, respectively, when $D_{\text{out}} = 80$ m with RISs. As D_{out} increases, the network sum rate decreases because the RISs gradually become distant from the BS and most of the UEs. Nevertheless, the proposed scheme still performs 5%, 8%, and 11% better than OPT PD-NOMA, MGF-NOMA, and SGF-NOMA schemes, respectively, when $D_{\text{out}} = 250$ m. We previously mentioned that an RIS could assist the other UEs in different clusters, even if its phases are aligned with the dedicated UE. This condition also helps further improve the network sum rate when the RIS is close to the BS.

As observed in Fig. 4.5(b), the network performance increases with R because more spectrum are available and more cluster becomes able to use an RIS. The proposed algorithm gives 8%, 12%, and 14% better performances than OPT PD-NOMA, MGF-NOMA, and SGF-NOMA, respectively.

Finally, Fig. 4.5(c) represents the sum rate of the network for varying N. The figure shows that the sum rate increases with N, similar to the case in Fig. 4.5(b). When proposed scheme is used, the network's performance is enhanced by 13%, 17%, and 20% for OPT PD-NOMA, MGF-NOMA, and SGF-NOMA, respectively. We emphasize that using $N = 30$ gives nearly the same sum rate as OPT PD-NOMA,

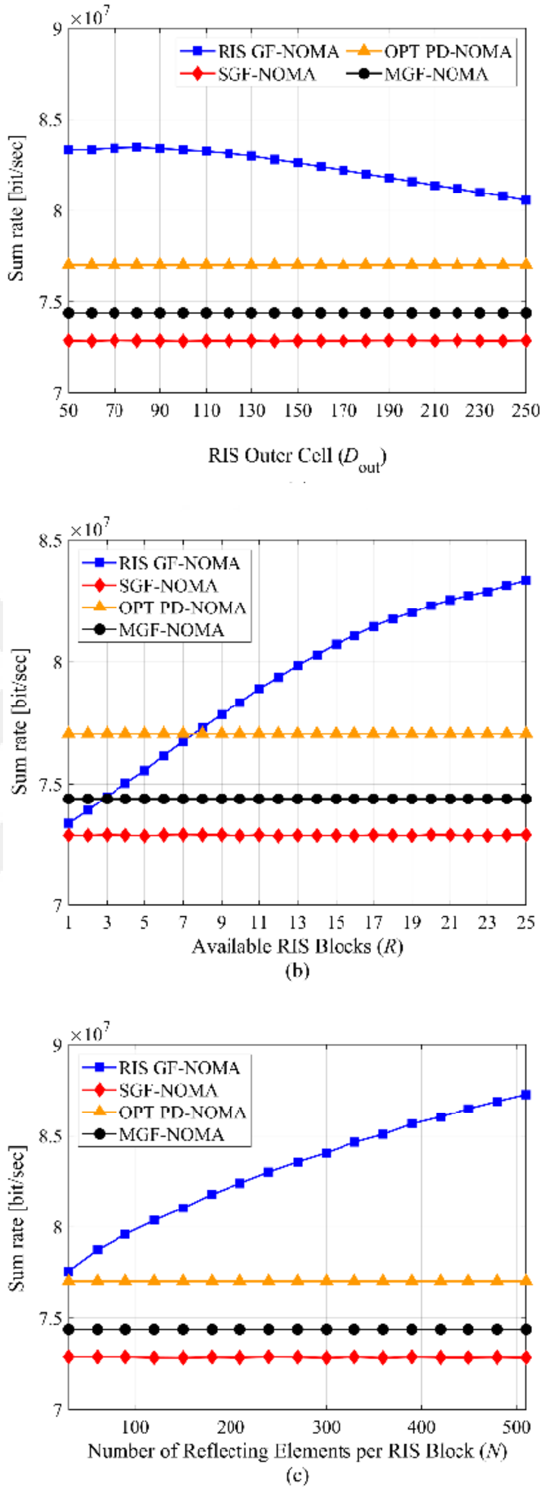

Figure 4.5: Sum rate of the network for different varying RIS metrics: (a) D_{out}, (b)R and (c)N.

meaning that we can achieve the same performance by using RISs with a very small number of reflecting elements.

4.2 Hybrid RIS-Empowered Reflection and Decode-and-Forward Relaying for Coverage Extension

In this section, the aim is to find the best transmission scenarios where RIS and relay work in harmony with each other. The relay can be considered as an additional performance-enhancing component to the RIS-assisted transmission scenario and the hybrid transmission can be conducted by activating the relay to compensate for rapid deterioration in the channel quality. The main motivation is to design hybrid RIS and relay-aided systems with low operational complexity, while keeping the advantages of RIS and relaying technologies. To this end, two different cost efficient scheme are proposed for coverage extension by avoiding multi-hop relaying, and the best positioning for the RIS and the relay are investigated by considering that the direct communication link between the end terminals is blocked [Yildirim et al., 2021a].

4.2.1 System and Channel Models

In this section, we present two different hybrid RIS & relay transmission scheme.

4.2.1.1 Joint RIS and Relay Transmission Scheme

The system model of the joint RIS and relay transmission scheme is illustrated in Fig. 4.6. As seen from Fig. 4.6, S and D are equipped with a single antenna and the channels between the S-D link and the S-relay link are not available due to the blockage. Since the signals at the millimeter and THz frequencies are highly vulnerable to the blockage, the reliability of transmission at high distances can be compromised. In this scenario, the coverage area of the communication is extended by placing an RIS in a position close to S, while it is aimed to reach the signal via the DF relay placed close to D.

In the first time-slot, the received signal at the relay and D are respectively given

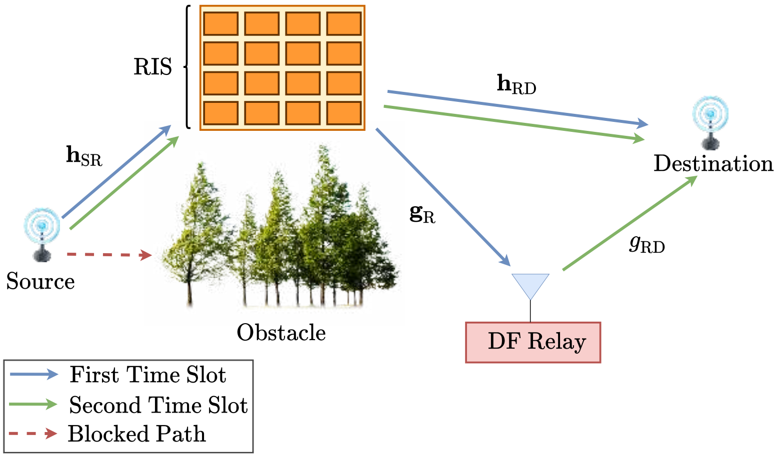

Figure 4.6: The system model of the joint RIS and DF relay transmission scheme where the RIS and the relay are placed close to the S and D, respectively.

by

$$y_{\mathrm{R}} = \sqrt{P_1}\mathbf{g}_{\mathrm{R}}^T \mathbf{\Phi}_1 \mathbf{h}_{\mathrm{SR}} s + n_{\mathrm{R}}, \tag{4.10}$$

$$y_{\mathrm{D}}^I = \sqrt{P_1}\mathbf{h}_{\mathrm{RD}}^T \mathbf{\Phi}_1 \mathbf{h}_{\mathrm{SR}} s + n_{\mathrm{D}}^I \tag{4.11}$$

where $\mathbf{g}_{\mathrm{R}} \in \mathbb{C}^{N\times 1}$, $\mathbf{h}_{\mathrm{SR}} \in \mathbb{C}^{N\times 1}$, and $\mathbf{h}_{\mathrm{RD}} \in \mathbb{C}^{N\times 1}$ are the fading channel coefficients between the RIS-relay, S-RIS, and RIS-D links, P_1 is the transmission power of S, $\mathbf{\Phi}_1 = \mathrm{diag}\left\{e^{j\phi_1^1}, \dots, e^{j\phi_1^N}\right\}$, with ϕ_1^i being the phase shift introduced by ith element of the RIS in the first time slot, s is the transmitted signal from S with unit-average-power ($\mathbb{E}[|s|^2] = 1$), n_{R} and n_{D}^I are the additive white Gaussian noise (AWGN) terms at the relay and D, which are distributed according to $\mathcal{CN}(0, N_0)$.

Assuming that the DF relay has a perfect decoding capability, the received signal at D in the second time slot can be expressed as follows:

$$y_{\mathrm{D}}^{II} = \sqrt{P_2}\mathbf{h}_{\mathrm{RD}}^T \mathbf{\Phi}_2 \mathbf{h}_{\mathrm{SR}} s + \sqrt{P_3} g_{\mathrm{RD}} s + n_{\mathrm{D}}^{II} \tag{4.12}$$

where $g_{\mathrm{RD}} \in \mathbb{C}$ is the fading channel coefficient between the relay-D link, P_2 and P_3 are respectively the transmission power of S and the relay in the second time slot, $\mathbf{\Phi}_2 = \mathrm{diag}\left\{e^{j\phi_2^1}, \dots, e^{j\phi_2^N}\right\}$, with ϕ_2^i being the phase shift of ith element of the RIS in the second time slot and n_{D}^{II} is the AWGN term distributed according to $\mathcal{CN}(0, N_0)$. In (4.12), the first term is denotes the RIS-based signal, while the second term represents the signal transmitted by the relay after perfectly decoded as s.

By considering intelligent phase shifting capability of the RIS, the maximized received SNR at D in the first time slot is expressed by

$$\gamma_1 = \max_{\mathbf{\Phi}_1} \frac{P_1 \left|\mathbf{h}_{\mathrm{RD}}^T \mathbf{\Phi}_1 \mathbf{h}_{\mathrm{SR}}\right|^2}{N_0} = \frac{P_1 \left|\sum_{i=1}^{N} |h_{\mathrm{RD,i}}||h_{\mathrm{SR,i}}|\right|^2}{N_0} = \frac{P_1 A^2}{N_0} \tag{4.13}$$

By considering the similar phase adjustment in the first time slot and assuming $P_2 = P_3$ due to simplicity, the maximized received SNR at the D in the second time slot is obtained as

$$\gamma_2 = \max_{\mathbf{\Phi}_2} \frac{P_2 \left|g_{RD} + \mathbf{h}_{\mathrm{RD}}^T \mathbf{\Phi}_2 \mathbf{h}_{\mathrm{SR}}\right|^2}{N_0} = \frac{P_2 \left||g_{RD}| + \sum_{i=1}^{N} |h_{\mathrm{RD,i}}||h_{\mathrm{SR,i}}|\right|^2}{N_0} = \frac{P_2 B^2}{N_0}. \tag{4.14}$$

4.2.1.2 Integrated RIS and Relay Transmission Scheme

In this hybrid scheme, we propose a transmission scheme where the RIS and the relay are integrated in the same device and positioned in between S and D as shown in Fig. 2. In contrast to the joint RIS and relaying scenario, we assume that S's signal reaches the RIS-relay device, which is both reflected and DF relayed to D. We again assume here that the distance between S and D is considerably large, hence, the S-D direct communication link is blocked.

In the first time-slot of the integrated RIS and relay transmission scheme, the received signal at the relay and D are respectively given by

$$y_{\mathrm{R}} = \sqrt{P_1} g_{\mathrm{SR}} s + n_{\mathrm{R}}, \tag{4.15}$$

$$y_{\mathrm{D}}^I = \sqrt{P_1} \mathbf{h}_{\mathrm{RD}}^T \mathbf{\Phi}_1 \mathbf{h}_{\mathrm{SR}} s + n_{\mathrm{D}}^I, \tag{4.16}$$

where $g_{\mathrm{SR}} \in \mathbb{C}$, $\mathbf{h}_{\mathrm{SR}} \in \mathbb{C}^{N\times 1}$ and $\mathbf{h}_{\mathrm{RD}} \in \mathbb{C}^{N\times 1}$ are the fading channel coefficients between the S-relay, S-RIS and RIS-D links, P_1 is the transmission power of S, s is the transmitted signal from S with the unit-average-power, n_{R} and n_{D}^I are the AWGN at the relay and D, which are distributed according to $\mathcal{CN}(0, N_0)$. The

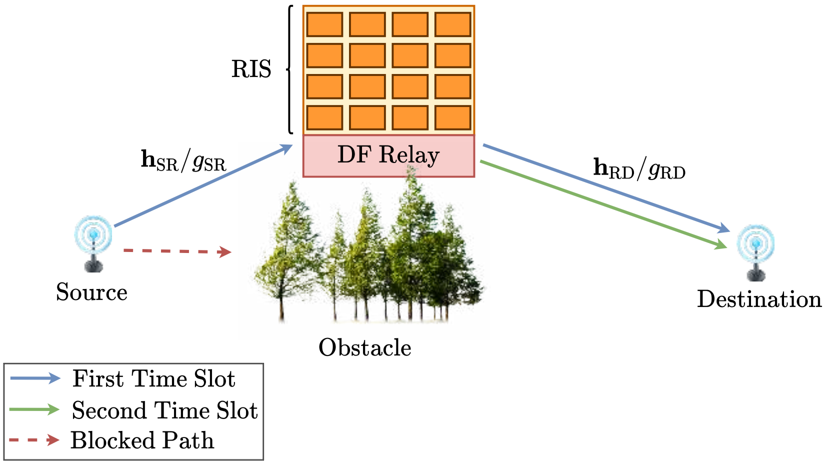

Figure 4.7: The system model of the integrated RIS and DF relay transmission scheme.

received signal transmitted through the perfect DF relay in the second time slot is obtained as

$$y_{\mathrm{D}}^{II} = \sqrt{P_2} g_{\mathrm{RD}} s + n_{\mathrm{D}}^{II}, \tag{4.17}$$

where g_{RD} is the fading channel coefficients between the relay-D link, $P_2$is the transmission power of relay in the second time slot, and n_{D}^{II} is the AWGN as $n \sim \mathcal{CN}(0, N_0)$.

Similar to the joint RIS and relay case, the received SNR in the first time slot is expressed as in (4.13).

4.2.2 Performance Analysis and Sequential Optimization

In this section, we analyze the achievable rate performance of our hybrid RIS and relay transmission schemes, and propose the sequential phase and power optimization algorithm in order to maximize the achievable rate under the non-ideal DF relay assumption. The decoding performance of the transmitted symbol degrades as the distance between the S and the relay increases. In this case, the transmit power may be adjusted to ensure that the maximized performance metrics are obtained.

Under the non-ideal DF relay, the achievable rate is calculated by

$$R_{\mathrm{Hybrid}}^{i} = 1/2 \log_2 \left(1 + \min\left\{\gamma_r^i, \gamma_{tot}\right\}\right), \; i \in \{1, 2\} \tag{4.18}$$

Algorithm 3 Sequential Phase and Power Optimization

```
if Joint RIS and relay transmission scheme then.
    Input: N_0, P_t, h_SR, h_RD, g_R, g_RD.
    Set P_2 = (P_t − P_1)/2.
    Optimize Φ_1 and Φ_2 by yielding the largest value of (4.13) and (4.14), respectively.
    Obtain A, B by using input channels, Φ_1 and Φ_2.
    Find optimal solution to P_1 and P_2 via CVX yielding the largest value of (4.19)
    return P_1, Φ_1, Φ_2.
else (Integrated RIS and relay transmission scheme)
    Input: N_0, P_t, h_SR, h_RD, g_SR, g_RD.
    Set P_2 = P_t − P_1.
    Optimize Φ_1 by yielding the largest value of (4.13).
    Obtain A by using input channels and Φ_1.
    Find optimal solution to P_1 and P_2 via CVX yielding the largest value of (4.20)
    return P_1, Φ_1
end if
```

where γ_r^1 and γ_r^2 is the received SNR at the relay for joint ($i = 1$) and integrated ($i = 2$) RIS and relay case. In order to obtain a maximized rate for the hybrid RIS and relay configuration in the joint RIS and relay transmission, the corresponding power optimization problem is formulated as

$$R^1_{\text{Hybrid}} = \max_{P_1} \quad \min\left(\frac{P_1|\mathbf{g}_{\text{R}}^T\mathbf{\Phi_1}\mathbf{h}_{\text{SR}}|^2}{N_0}, \frac{P_2\text{A}^2}{N_0} + \frac{P_2\text{B}^2}{N_0}\right) \qquad \text{s.t.} \quad P_2 = (P_{\text{tot}} - P_1)/2, \quad P_1 < P_{\text{tot}} \tag{4.19}$$

Here, we assumed that $P_2 = P_3$ to have a convex optimization problem. Thus, the power constraint in (4.19) is set by considering $P_t = P_1 + 2P_2$. The corresponding optimization problem for integrated RIS and relay case at D in the second time slot is expressed as

$$R^2_{\text{Hybrid}} = \max_{P_1} \quad \min\left(\frac{P_1|g_{\text{SR}}|^2}{N_0}, \frac{P_2\text{A}^2}{N_0} + \frac{P_2\,|g_{\text{RD}}|^2}{N_0}\right) \qquad \text{s.t.} \quad P_2 = P_{\text{tot}} - P_1, \quad P_1 < P_{\text{tot}} \tag{4.20}$$

Since S does not transmit in both time slots for the integrated RIS and relay scheme, the power constraint in (4.20) is set by considering $P_t = P_1 + P_2$. Here, the total power should be allocated between first and second time slots, in order to enhance

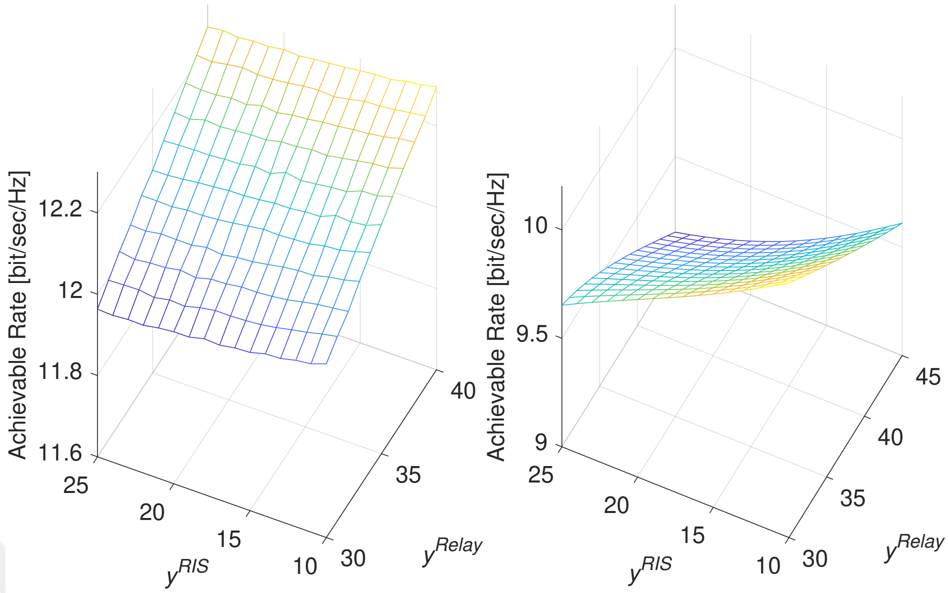

(a) **(b)**

Figure 4.8: Achievable rate of the joint RIS and relay scheme when (a) ideal and (b) non-ideal relaying are considered for a varying distance in the y-axis between the RIS and the DF relay.

system performance. To this end, sequential phase and power optimization algorithm is proposed to sequentially optimize the phase responses of the RIS elements and transmit powers in order to obtain the maximized rate. In this algorithm, the inputs are selected according to corresponding concept. First, $\mathbf{\Phi_1}$ and $\mathbf{\Phi_2}$ are optimized to maximize the received SNR in both time slots. Then, using this phase matrices, end-to-end channel expressions are obtained to modify SNR expressions. In the last step, the optimal value of P_1 is calculated by using the CVX tool [Grant and Boyd, 2014] to maximize the rate and iteratively search for this optimal value until the objective function converges. Here, the complexity of Algorithm 1 depends on the number of iterations. The overall steps of the sequential algorithm to solve (4.19) and (4.20) are summarized in Algorithm 1.

4.2.3 Numerical Results

In this section, we illustrate the error and achievable rate performances of the proposed hybrid schemes via numerical simulations by considering path loss as well as channel fading. Rician factor is assumed as $K = 10$ dB for all simulations, and path

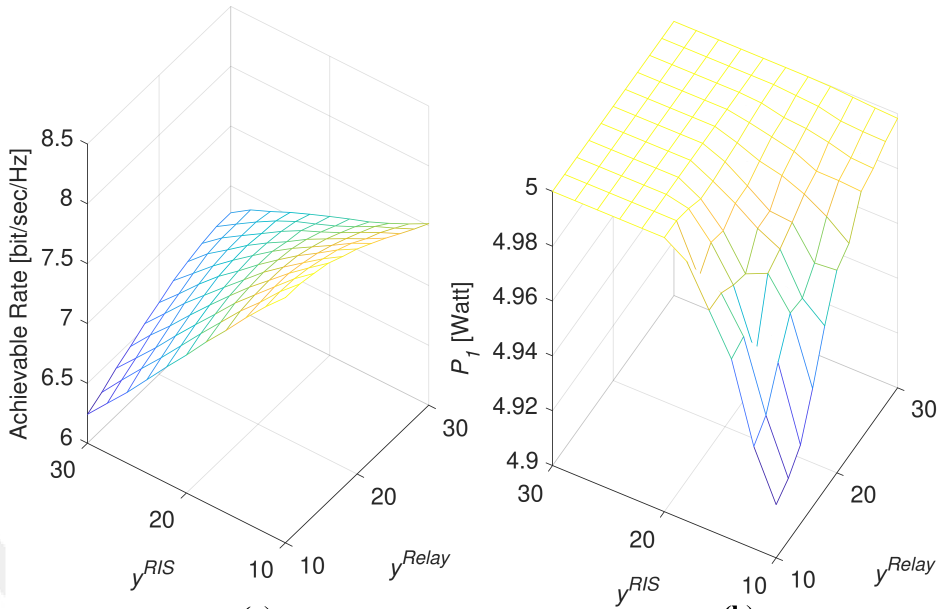

(a) **(b)**

Figure 4.9: (a) Achievable rate and (b) P_1 analysis for the joint RIS and relay transmission with the sequential algorithm for $N = 1024$ at 28 GHz.

loss is modeled using the 3GPP Urban Micro (UMi) [3GP, 2010] and 5G UMi-Street Canyon [Sun *et al.*, 2016] path loss models for 2.4 GHz and 28 GHz, respectively. Here, we consider a two-dimensional (2D) coordinate system for the positioning of the terminals, which are located in the xy-plane. In Figs. 4.8(a) and (b), the effect of varying RIS and relay positions in the y-axis on the achievable rate performance of the joint RIS and relay transmission scheme is investigated under perfect and imperfect DF relay assumption for $P_1 = 5$ W, $P_2 = 2.5$ W, $N_0 = -130$ dBm and $N = 2048$ at 28 GHz. Here, the S, D, RIS, and the relay are located at $(10, 0)$, $(10, 60)$, $(0, y^{\text{RIS}})$ and $(25, y^{\text{Relay}})$ in the xy-plane, respectively. As seen from Fig. 4.8(a), the best achievable rate performance is obtained when the RIS is close to S and the relay is close to D, while the proximity of the ideal relay to D is a more dominant factor in this scheme. On the other hand, as seen in Fig. 4.8(b), since the RIS plays a more effective role in transmission when the relay does not have perfect decoding capability, the best achievable rate performance is obtained when the RIS is close to the S and the relay close to the RIS. In other words, the existence of a reliable channel between the RIS-relay will play a key role in achievable rate under the non-ideal relay.

As shown from Fig. 4.9(a), the achievable rate is maximized when both the RIS and the relay are positioned close to S. If the RIS is positioned far from S, the signal quality at the relay will be deteriorated considerably. Since the perfect decoding assumption is not considered, the signal quality at the relay increases as the relay is located closer to the RIS, therefore, the required P_1 decreases, and more power is assigned to the second-time slot, as seen from Fig. 4.9(b). In other words, the rate is maximized when the relay is activated and more power assigned to P_2.

Chapter 5

CONCLUSION

In this thesis, first, a physical channel model for RIS-assisted networks is presented in sub-6 GHz frequency bands. This study aims to meet the lack of analysis of RIS-assisted systems for sub-6 GHz bands in the literature by considering physical channels in sub-6 GHz bands. The performance of the system is analyzed from different perspectives, such as different environments, locations of the Tx, Rx and RIS, operating frequencies, number of RIS elements for near-field and far-field conditions. Our future works may include the extension of this work to MIMO systems along with real-world experimental results.

This thesis has also proposed two iterative clustering algorithms with 3D and 2D assignment approaches for an RIS-assisted GF-NOMA system. The performance of RISs have been considered to boost the capacity of a GF-NOMA system. Through the proposed algorithms, the network can leverage RIS assistance to create received power disparity among NOMA UEs without the need for complex power control. Also, Algorithm 2 has been found to be faster and superior to Algorithm 1 in terms of complexity. Moreover, assisting the system with RISs results in better SIC due to the power disparity introduced from the presence of the RISs, leading to improved achievable rates compared with the conventional GF-NOMA with no RIS assistance. Additionally, GF-NOMA schemes with identical transmit power have been shown to provide more fairness among UEs in a cluster in terms of energy efficiency. Future works can consider assisting not only one UE but multiple UEs in a cluster and the multiple cell scenarios where UEs are also jointly assigned to the BSs, which can come up with some complex optimization problems.

Finally, two hybrid transmission concepts have been proposed to improve achievable rate and error performance by exploiting the most important advantages of RIS and relaying technologies. Although, most of the previous works consider RISs and relaying as rivals to each other, we have shown by extensive numerical studies that these two exciting technologies can work in a harmony with each other under appropriate transmission scenarios. It is also demonstrated through simulations that the relay can be considered as an additional performance-enhancing component to the RIS-assisted transmission scenario especially in the case of rapid deterioration in the channel.

BIBLIOGRAPHY

[3GP, 2010] (2010). *Evolved Universal Terrestrial Radio Access (E-UTRA);Further Advancements for E-UTRA Physical Layer Aspects*. 3GPP-TR-36.814.

[3GP, 2017] (2017). 3GPP TR 36.873 V12.7.0 - Study on 3D channel model for LTE.

[3GP, 2019] (2019). 3GPP TR 38.901 V16.1.0 - Study on channel model for frequencies from 0.5 to 100 GHz.

[Abbas et al., 2019] Abbas, R., Shirvanimoghaddam, M., Li, Y., and Vucetic, B. (2019). A novel analytical framework for massive grant-free noma. *IEEE Trans. Commun.*, 67(3):2436–2449.

[Abdallah et al.,] Abdallah, A., Celik, A., Mansour, M. M., and Eltawil, A. M. Deep learning-based channel estimation for wideband RIS-aided mmWave MIMO system with beam squint. Accepted to appear in ICC 2022.

[Abdullah *et al.*, 2020a] Abdullah *et al.*, Z. (2020a). A hybrid relay and intelligent reflecting surface network and its ergodic performance analysis. *IEEE Wireless Commun. Lett.*, 9(10):1653–1657.

[Abdullah *et al.*, 2020b] Abdullah *et al.*, Z. (2020b). Optimization of intelligent reflecting surface assisted full-duplex relay networks. *IEEE Wireless Commun. Lett. (Early Access)*.

[Aldababsa et al., 2021] Aldababsa, M., Khaleel, A., and Basar, E. (2021). Simultaneous transmitting and reflecting intelligent surfaces-empowered NOMA networks.

[Aldababsa et al., 2022] Aldababsa, M., Khaleel, A., and Basar, E. (2022). STAR-RIS-NOMA networks: An error performance perspective. *IEEE Commun. Lett.*, pages 1–1. (early access).

[Arslan et al., 2020] Arslan, E., Dogukan, A. T., and Basar, E. (2020). Index modulation-based flexible non-orthogonal multiple access. *IEEE Wireless Commun. Lett.*, 9(11):1942–1946.

[Arslan et al., 2022] Arslan, E., Yildirim, I., Kilinc, F., and Basar, E. (2022). Over-the-air equalization with reconfigurable intelligent surfaces. *IET Commun.*

[Arzykulov et al., 2022] Arzykulov, S., Celik, A., Nauryzbayev, G., and Eltawil, A. M. (2022). UAV-assisted cooperative & cognitive NOMA: Deployment, clustering, and resource allocation. *IEEE Trans. Cogn. Commun.*, 8(1):263–281.

[Arzykulov et al., 2021] Arzykulov, S., Nauryzbayev, G., Celik, A., and Eltawil, A. M. (2021). Hardware and interference limited cooperative CR-NOMA networks under imperfect SIC and CSI. *IEEE Open J. Commun. Soc.*, 2:1473–1485.

[Balanis, 2016] Balanis, C. A. (2016). *Antenna Theory Analysis and Design.* Wiley, USA.

[Balevi et al., 2018] Balevi, E., Rabee, F. T. A., and Gitlin, R. D. (2018). ALOHA-NOMA for massive machine-to-machine IoT communication. In *2018 IEEE Int. Conf. Commun. (ICC)*, pages 1–5.

[Basar, 2020] Basar, E. (2020). Reconfigurable intelligent surface-based index modulation: A new beyond MIMO paradigm for 6G. *IEEE Trans. Commun.*, 68(5):3187–3196.

[Basar et al., 2019] Basar, E., Di Renzo, M., De Rosny, J., Debbah, M., Alouini, M.-S., and Zhang, R. (2019). Wireless communications through reconfigurable intelligent surfaces. *IEEE Access*, 7:116753–116773.

[Basar and Yildirim, 2020] Basar, E. and Yildirim, I. (2020). Indoor and outdoor physical channel modeling and efficient positioning for reconfigurable intelligent surfaces in mmWave bands.

[Basar and Yildirim, 2020] Basar, E. and Yildirim, I. (2020). SimRIS channel simulator for reconfigurable intelligent surface-empowered communication systems. In *2020 IEEE Latin-American Conf. Commun. (LATINCOM)*, pages 1–6.

[Basar et al., 2021] Basar, E., Yildirim, I., and Kilinc, F. (2021). Indoor and outdoor physical channel modeling and efficient positioning for reconfigurable intelligent surfaces in mmWave bands. *IEEE Trans. Commun.*, 69(12):8600–8611.

[Björnson and Sanguinetti, 2020] Björnson, E. and Sanguinetti, L. (2020). Power scaling laws and near-field behaviors of massive MIMO and intelligent reflecting surfaces. *IEEE OJ-COMS*, 1:1306–1324.

[Björnson et al., 2020] Björnson, E., Ozdogan, O., and Larsson, E. G. (2020). Intelligent reflecting surface versus decode-and-forward: How large surfaces are needed to beat relaying? *IEEE Wireless Commun. Lett.*, 9(2):244–248.

[Björnson and Sanguinetti, 2020] Björnson, E. and Sanguinetti, L. (2020). Rayleigh fading modeling and channel hardening for reconfigurable intelligent surfaces.

[Celik, 2021] Celik, A. (2021). Grant-free NOMA: A low complexity power control through user clustering.

[Chen et al., 2022] Chen, J., Guo, L., Jia, J., Shang, J., and Wang, X. (2022). Resource allocation for IRS assisted SGF NOMA transmission: A MADRL approach. *IEEE J. Sel. Areas Commun.*, 40(4):1302–1316.

[Chen et al., 2021] Chen, Q., Li, M., Yang, X., Alturki, R., Alshehri, M. D., and Khan, F. (2021). Impact of residual hardware impairment on the IoT secrecy performance of RIS-assisted NOMA networks. *IEEE Access*, 9:42583–42592.

[C.Pan *et al.*, 2021] C.Pan *et al.* (2021). Reconfigurable intelligent surfaces for 6G systems: Principles, applications, and research directions. *IEEE Commun. Mag.*, 59(6):14–20.

[Di Renzo *et al.*, 2019] Di Renzo *et al.*, M. (2019). Smart radio environments empowered by reconfigurable ai meta-surfaces: An idea whose time has come. *EURASIP J. Wireless Commun. and Netw.*, 2019(1):1–20.

[Doğan et al., 2019] Doğan, S., Tusha, A., and Arslan, H. (2019). NOMA with index modulation for uplink URLLC through grant-free access. *IEEE J. Sel. Topics Signal Process.*, 13(6):1249–1257.

[Elhattab et al., 2021] Elhattab, M., Arfaoui, M.-A., Assi, C., and Ghrayeb, A. (2021). Reconfigurable intelligent surface assisted coordinated multipoint in downlink NOMA networks. *IEEE Commun. Lett.*, 25(2):632–636.

[Elkourdi et al., 2018] Elkourdi, M., Mazin, A., Balevi, E., and Gitlin, R. D. (2018). Enabling slotted aloha-NOMA for massive m2m communication in IoT networks. In *IEEE 19th Wireless Microw. Technol. Conf. (WAMICON)*, pages 1–4.

[Fayaz et al., 2021] Fayaz, M., Yi, W., Liu, Y., and Nallanathan, A. (2021). Transmit power pool design for grant-free NOMA-IoT networks via deep reinforcement learning. *IEEE Trans. Wireless Commun.*, 20(11):7626–7641.

[Grant and Boyd, 2014] Grant, M. and Boyd, S. (2014). CVX: Matlab software for disciplined convex programming, version 2.1. `http://cvxr.com/cvx`.

[Hemadeh et al., 2018] Hemadeh, I. A., Satyanarayana, K., El-Hajjar, M., and Hanzo, L. (2018). Millimeter-wave communications: Physical channel models, design considerations, antenna constructions, and link-budget. *IEEE Commun. Surveys Tuts.*, 20(2):870–913.

[Hemanth et al., 2020] Hemanth, A., Umamaheswari, K., Pogaku, A. C., Do, D.-T., and Lee, B. M. (2020). Outage performance analysis of reconfigurable intelligent surfaces-aided NOMA under presence of hardware impairment. *IEEE Access*, 8:212156–212165.

[Hou et al., 2020a] Hou, T., Liu, Y., Song, Z., Sun, X., Chen, Y., and Hanzo, L. (2020a). Reconfigurable intelligent surface aided NOMA networks. *IEEE J. Sel. Areas Commun.*, 38(11):2575–2588.

[Hou et al., 2020b] Hou, T., Liu, Y., Song, Z., Sun, X., Chen, Y., and Hanzo, L. (2020b). Reconfigurable intelligent surface aided noma networks. *IEEE J. Sel. Areas Commun.*, 38(11):2575–2588.

[Huang *et al.*, 2019] Huang *et al.*, C. (2019). Reconfigurable intelligent surfaces for energy efficiency in wireless communication. *IEEE Trans. Wireless Commun.*, 18(8):4157–4170.

[Huang *et al.*, 2020] Huang *et al.*, C. (2020). Holographic MIMO surfaces for 6G wireless networks: Opportunities, challenges, and trends. *IEEE Wireless Commun.*, 27(5):118–125.

[Islam et al., 2017] Islam, S. M. R., Avazov, N., Dobre, O. A., and Kwak, K.-s. (2017). Power-domain non-orthogonal multiple access (NOMA) in 5G systems: Potentials and challenges. *IEEE Commun. Surv.*, 19(2):721–742.

[Khaleel and Basar, 2022] Khaleel, A. and Basar, E. (2022). A novel NOMA solution with RIS partitioning. *EEE J. Sel. Top. Signal Process.*, 16(1):70–81.

[Kılınç et al., 2022] Kılınç, F., Tasci, R. A., Celik, A., Abdallah, A., Eltawil, A., and Basar, E. (2022). Ris-assisted grant-free noma: User pairing, ris assignment, and phase shift alignment.

[Kilinc et al., 2021] Kilinc, F., Yildirim, I., and Basar, E. (2021). Physical channel modeling for RIS-empowered wireless networks in sub-6 GHz bands : (invited paper). In *2021 55th Asilomar Conf. on Signals Syst. Comput.*, pages 704–708.

[Kyösti *et al.*, 2008] Kyösti *et al.*, P. (2008). WINNER II channel models. *IST-4-027756 WINNER II D1.1.2 V1.2.*

[Liu et al., 2021a] Liu, J., Wu, G., Zhang, X., Fang, S., and Li, S. (2021a). Modeling, analysis, and optimization of grant-free NOMA in massive MTC via stochastic geometry. *IEEE Internet Things J.*, 8(6):4389–4402.

[Liu et al., 2021b] Liu, X., Liu, Y., Chen, Y., and Poor, H. V. (2021b). RIS enhanced massive non-orthogonal multiple access networks: Deployment and passive beamforming design. *IEEE J. Sel. Areas Commun.*, 39(4):1057–1071.

[Liu et al., 2022] Liu, Y., Mu, X., Liu, X., Di Renzo, M., Ding, Z., and Schober, R. (2022). Reconfigurable intelligent surface-aided multi-user networks: Interplay between NOMA and RIS. *IEEE Wireless Commun.*, 29(2):169–176.

[M.Di Renzo *et al.*, 2020] M.Di Renzo *et al.* (2020). Reconfigurable intelligent surfaces vs. relaying: Differences, similarities, and performance comparison. *IEEE Open J. Commun. Soc.*, 1:798–807.

[Nayeri et al., 2018a] Nayeri, P., Yang, F., and Elsherbeni, A. Z. (2018a). *Reflectarray Antennas: Theory, Designs, and Applications.* Wiley, USA.

[Nayeri et al., 2018b] Nayeri, P., Yang, F., and Elsherbeni, A. Z. (2018b). *Reflectarray Antennas: Theory, Designs, and Applications.* Wiley, USA.

[Pattipati et al., 1992] Pattipati, K., Deb, S., Bar-Shalom, Y., and Washburn, R. (1992). A new relaxation algorithm and passive sensor data association. *IEEE Trans. Autom. Control*, 37(2):198–213.

[Saito et al., 2013] Saito, Y., Kishiyama, Y., Benjebbour, A., Nakamura, T., Li, A., and Higuchi, K. (2013). Non-orthogonal multiple access (NOMA) for cellular future radio access. In *2013 IEEE 77th Veh. Technol. Conf.*, pages 1–5.

[Shahab et al., 2020] Shahab, M. B., Abbas, R., Shirvanimoghaddam, M., and Johnson, S. J. (2020). Grant-free non-orthogonal multiple access for IoT: A survey. *IEEE Commun. Surv. Tutor.*, 22(3):1805–1838.

[Sun *et al.*, 2016] Sun *et al.*, S. (2016). Propagation path loss models for 5G urban micro- and macro-cellular scenarios. In *Proc. 2016 IEEE 83rd Veh. Technol. Conf. (VTC Spring)*, pages 1–6.

[Tang et al., 2021] Tang, Z., Hou, T., Liu, Y., Zhang, J., and Zhong, C. (2021). A novel design of RIS for enhancing the physical layer security for RIS-aided NOMA networks. *IEEE Wireless Commun. Lett.*, 10(11):2398–2401.

[Tasci et al., 2022] Tasci, R. A., Kilinc, F., Celik, A., Abdallah, A., Eltawil, A. M., and Basar, E. (2022). Ris-assisted grant-free noma. *arXiv preprint arXiv:2207.11531*.

[Wu et al., 2021] Wu, Q., Zhang, S., Zheng, B., You, C., and Zhang, R. (2021). Intelligent reflecting surface-aided wireless communications: A tutorial. *IEEE Trans. Commun.*, 69(5):3313–3351.

[Yang et al., 2021a] Yang, G., Xu, X., Liang, Y.-C., and Renzo, M. D. (2021a). Reconfigurable intelligent surface-assisted non-orthogonal multiple access. *IEEE Trans. Wireless Commun.*, 20(5):3137–3151.

[Yang et al., 2021b] Yang, Z., Liu, Y., Chen, Y., and Al-Dhahir, N. (2021b). Machine learning for user partitioning and phase shifters design in RIS-aided NOMA networks. *IEEE Trans. Commun.*, 69(11):7414–7428.

[Yildirim et al., 2021a] Yildirim, I., Kilinc, F., Basar, E., and Alexandropoulos, G. C. (2021a). Hybrid RIS-empowered reflection and decode-and-forward relaying for coverage extension. *IEEE Commun. Lett.*, 25(5):1692–1696.

[Yildirim et al., 2020] Yildirim, I., Uyrus, A., and Basar, E. (2020). Modeling and analysis of reconfigurable intelligent surfaces for indoor and outdoor applications in future wireless networks. *IEEE Trans. Commun. (Early access)*.

[Yildirim et al., 2021b] Yildirim, I., Uyrus, A., and Basar, E. (2021b). Modeling and analysis of reconfigurable intelligent surfaces for indoor and outdoor applications in future wireless networks. *IEEE Trans. Commun.*, 69(2):1290–1301.

[Ying et al., 2020] Ying, X., Demirhan, U., and Alkhateeb, A. (2020). Relay aided intelligent reconfigurable surfaces: Achieving the potential without so many antennas.

[Zhang et al., 2022] Zhang, C., Liu, Y., and Ding, Z. (2022). Semi-grant-free NOMA: A stochastic geometry model. *IEEE Trans. Wireless Commun.*, 21(2):1197–1213.

[Zhang et al., 2020] Zhang, C., Qin, Z., Liu, Y., and Chai, K. K. (2020). Semi-grant-free uplink NOMA with contention control: A stochastic geometry model. In *2020 IEEE Int. Conf. Commun. (ICC) Workshops (ICC Workshops)*, pages 1–6.

[Zhang and Zhang, 2020] Zhang, S. and Zhang, R. (2020). Capacity characterization for intelligent reflecting surface aided MIMO communication. *IEEE J. Sel. Areas Commun.*, 38(8):1823–1838.

[Zhang et al., 2021] Zhang, Z., Zhang, C., Jiang, C., Jia, F., Ge, J., and Gong, F. (2021). Improving physical layer security for reconfigurable intelligent surface aided NOMA 6G networks. *IEEE Trans. Veh. Tech.*, 70(5):4451–4463.

[Zhong et al., 2022] Zhong, R., Liu, Y., Mu, X., Chen, Y., and Song, L. (2022). AI empowered RIS-assisted NOMA networks: Deep learning or reinforcement learning? *IEEE J. Sel. Areas Commun.*, 40(1):182–196.